



## OPEN Anisotropic crack evolution and fractal failure mechanism of Lushan shale under compression: insights from acoustic emission

Huasen Huang, Yu Zhou, Yongfa Zhang✉, Chunlin Wang & Jin Bi

The Lushan shale, located in the Upper Sinian Formation of China, is a promising zone for commercial shale gas development. Understanding the crack evolution and fractal failure mechanisms of anisotropic Lushan shale under compression is critical for ensuring safe drilling and optimizing reservoir reconstruction. In this study, uniaxial compression tests were conducted on Lushan shale samples with varying bedding angles ( $\vartheta$ ) ranging from  $0^\circ$  to  $90^\circ$ , using acoustic emission (AE) techniques to monitor crack propagation and failure processes. The results reveal that both uniaxial compressive strength (UCS) and cumulative AE counts initially decrease and then increase with increasing bedding angle, reaching a minimum at  $\vartheta = 60^\circ$ . During the initial loading phase, microcracking activity predominates, as indicated by a rising AE amplitude (*b*-value); however, as the stress nears 70–80% of the UCS, the *b*-value undergoes a sharp decline, signaling a corresponding surge in large-magnitude cracking events and the onset of rock instability. Regardless of varying bedding angles, the failure of Lushan shale under compression is primarily dominated by tensile fractures, accounting for over 70% of the total fracture events. Three failure modes of anisotropic shale were mainly identified: through-layer failure, layer-slip failure, and tensile splitting failure. Fractal statistical analysis reveals that the fractal dimensions of AE signals correlate with shale fragment distribution, indicating that microcracking evolution directly influences macroscopic failure patterns, providing a potential framework for assessing rock stability.

**Keywords** Lushan shale, Acoustic emission, Bedding anisotropy, Failure mode, Compression

### List of symbols

A	Amplitude (dB)
a	Empirical constant
b	AE <i>b</i> -value
D	Duration ( $\mu$ s)
$D_{AE}$	AE correlation dimension
$D_f$	fractal dimension
$H(u)$	Heaviside function
k	Maximum ordinate value/maximum abscissa value
$k_{sf}$	Scaling factor
$L_{eq}$	Equivalent side length converted
$L_{eqmax}$	Maximum equivalent side length
$M^*$	Earthquake magnitude exceeding
n	Dimension of the reconstructed phase space
N	Total number of the events
$N_f$	Number of fragments
$N_0$	Number of fragments with the largest feature scale
r	Given scaling function
$W(r)$	Correlation dimension
X	Vector of the reconstructed phase space

College of Civil Engineering, Guizhou University, Huaxi District, Guiyang 550025, Guizhou, China. ✉email: zyfcqu@126.com

**Greek letters**

$\theta$	Bedding angle (°)
$\sigma$	Average UCS (MPa)
$\sigma_n$	Normal stress
$\tau$	Shear stress

**Abbreviations**

AC	AE count
AE	Acoustic emission
AF	Average frequency (kHz)
ISRM	International Society for Rock Mechanics
RA	Rising angle (ms/v)
RT	Rise time ( $\mu$ s)
UCS	Uniaxial compressive strength (MPa)
XRD	X-ray diffraction

As an invaluable unconventional energy resource, shale gas plays a crucial role in mitigating the ongoing energy crisis<sup>1,2</sup>. The extraction of shale gas via hydraulic fracturing involves the excavation and reconstruction of shale buried several kilometers deep, where the shale may undergo severe compression and fracture process. The resistance of shale against compression plays a vital role in rock fracture mechanics and is closely linked to fracture failure<sup>3–8</sup>. The accurate evaluation of the properties of a target shale reservoir is critical to various aspects of field operations. However, due to distinctions in the diagenetic environment and sedimentary history among different shale formations, the mechanical properties of shale reservoirs may vary significantly across different sampling locations<sup>9</sup>. While recent studies have placed increasing focus on the Longmaxi shale<sup>10–13</sup>, the shale of the Sinian formation in southern China (e.g., Lushan shale) has received limited attention in comparison. The anisotropic fracture behavior associated with beddings can also disturb the formation of fracture network. The variability of rock properties should be considered in actual oil and gas recovery<sup>14–16</sup>. Therefore, gaining an in-depth understanding of the anisotropic crack evolution and failure of characteristics Lushan shale under compression is of great significance for the subsequent design of hydraulic fracturing operations.

Understanding the anisotropy of shale bedding planes is crucial for shale-related engineering activities such as hydraulic fracturing, drilling, and underground excavation. Huang et al.<sup>17</sup> analyzed effective methods for evaluating shale gas reservoir production performance, including the decline pattern of production and the prediction of ultimate recovery rate. Ardebili et al.<sup>18</sup> utilized artificial intelligence to estimate shale porosity and volume in a case study of the Kashafrud Gas Reservoir located in Northeast Iran. Yang et al.<sup>19</sup> conducted numerical simulations of Brazilian splitting of shale using CT scanning technology combined with finite element software. Esatyana et al.<sup>20</sup> proposed a conceptual model that utilizes nanoindentation at the sub-centimeter scale to characterize the anisotropic fracture toughness of shale. The aforementioned research conducted by these scholars is all based on the condition of shale, which underscores the necessity of studying the structural and mechanical characteristics of shale. The aforementioned research conducted by scholars mainly focused on the failure characteristics of Longmaxi shale and Niutitang shale. However, the Lushan shale, serving as a potential commercial development zone for shale gas<sup>21,22</sup>, exhibit distinct physical properties relative to previous shales<sup>23</sup>, but has received limited attentions. Therefore, this paper undertakes a comprehensive investigation on Lushan shale as the research backdrop, aiming to enhance hydraulic fracturing performance.

The fracture process in rock can be intuitively reflected by the evolution of acoustic emission (AE) signals. Extensive research has been conducted by numerous scholars to investigate the AE characteristics associated with shale failure. For example, Zhang et al.<sup>24</sup> carried out the laboratory hydraulic fracturing of shale and analyzed the AE evolution characteristics. Through the amplitude and frequency analysis of acoustic signals, they found that the failure of Changning shale is dominated by tensile fractures during loading process. Zhang et al.<sup>25</sup> found that the wellbore direction has a more significant influence on the breakdown pressure than bedding angles, but with increasing bedding inclination angle, its influence gradually weakens. Zhang et al.<sup>26</sup> conducted six hydraulic fracturing tests on shale with different bedding angles, which reported that the fracture initiation pressure and fracture pressure increased first and then decreased with the increase of bedding angle, and there is a strong linear correlation between them, independent of shale heterogeneity. Zhao et al.<sup>27</sup> explored the fracture mechanism of sandstone subjected to three-point bending loading based on AE count analysis. Zhang et al.<sup>28</sup> carried out a series of hydraulic fracturing experiments on shale with various beddings inclinations and found three evolutionary trends of cumulative AE counts. Wu et al.<sup>29</sup> demonstrated the feasibility of using RA and AF values to identify different types of cracks in tunnel monitoring. These studies demonstrate that the evolution of AE characteristic parameters during the process of rock failure can provide valuable insights into the fracture details of the rock. However, in the research on shale-related engineering activities<sup>30–32</sup>, most scholars rarely conduct an analysis and understanding of the anisotropic crack evolution and fractal failure mechanism of shale samples under compression. Additionally, merely analyzing a single AE parameter is insufficient to fully comprehend the failure mechanism of shale.

In this paper, a series of uniaxial compression tests are carried out on the combined acoustic emission of Lushan shale, the anisotropic crack evolution and fractal failure mechanism of Lushan shale under compression are expounded, and the correspondence between acoustic emission parameters at each stage of compression process and shale macroscopic failure fractures was studied, and the rationality of acoustic emission parameters was verified. The research results can provide important reference for the subsequent development and design of on-site hydraulic fracturing.

## Materials and methods

### Samples preparation

The shale used in this study was sourced from the outcrops of the upper Sinian formation in Lushan City, Jiangxi Province, China (Fig. 1a). All samples were taken from a single shale block to reduce experimental errors due to component differences. After removing the weathered surfaces, the shale blocks were processed into standard cylinders ( $\Phi 50 \times 100$  mm) with different bedding angles  $\theta$  of  $0^\circ$ ,  $30^\circ$ ,  $45^\circ$ ,  $60^\circ$  and  $90^\circ$ , where  $\theta$  is the angle formed by the bedding plane and the horizontal plane, as shown in Fig. 1b-d. The parallelism of the upper and lower surfaces of the specimen was controlled within a tolerance of 0.05 mm, while the surface flatness achieved a precision level of 0.02 mm. The machining accuracy of all specimens complies the requirements recommended by the International Society for Rock Mechanics (ISRM). Through X-Ray Diffraction (XRD) mineral composition, as shown in Fig. 2a. The mineral composition of the shale includes illite (40.7%), quartz (25.4%), albite (8.7%), muscovite (6.6%), calcite (2.5%), kaolinite (1%), and clinocllore (15.1%), as shown in Fig. 2b. The permeability and porosity of the specimen at room temperature were  $1.04 \pm 0.11$  ( $10^{-3}$  mD) and  $1.53\% \pm 0.59$  (%), respectively.

Additionally, prior to conducting the experiment, a wave velocity tester, depicted in Fig. 3, was employed for the purpose of accurately measuring the longitudinal wave velocity within shale samples. The results were summarized in Table 1. To minimize the errors caused by sampling variability and artificial processing, three samples with approximately equivalent P-wave velocity were selected for each testing condition.

### Experimental equipment

As shown in Fig. 4, the experimental equipment consists of an axial loading system and an acoustic emission system. The vertical load is applied by the DSZ-1000 rock triaxial testing machine, which has the maximum load capacity of 1000 kN, the maximum axial displacement of 50 mm, and the minimum measurement accuracy of 0.25%FS. The axial loading rate can be adjusted within 0.1–100 mm/min. Data can be recorded in real time according to the predetermined time period, peak force or loading rate. The acoustic emission system belongs to a Mirco-II Express acoustic emission system and is manufactured by Physical Acoustic Corporation (PAC), which has a 16-bit/A/D architecture, a maximum bandwidth of 1.2 MHz, and a maximum signal amplitude of 100 dB. This enables continuous acquisition of multi-channel AE signals during loading. To avoid ambient noise, the AE hardware is set up with a pre-amplification of 40 dB, a threshold is 40 dB, and a sampling rate of 5 MSPS.

### Experimental procedure

In order to explore the AE evolution and failure characteristics of various anisotropic shale specimens under uniaxial compression, the following steps are performed in this paper:

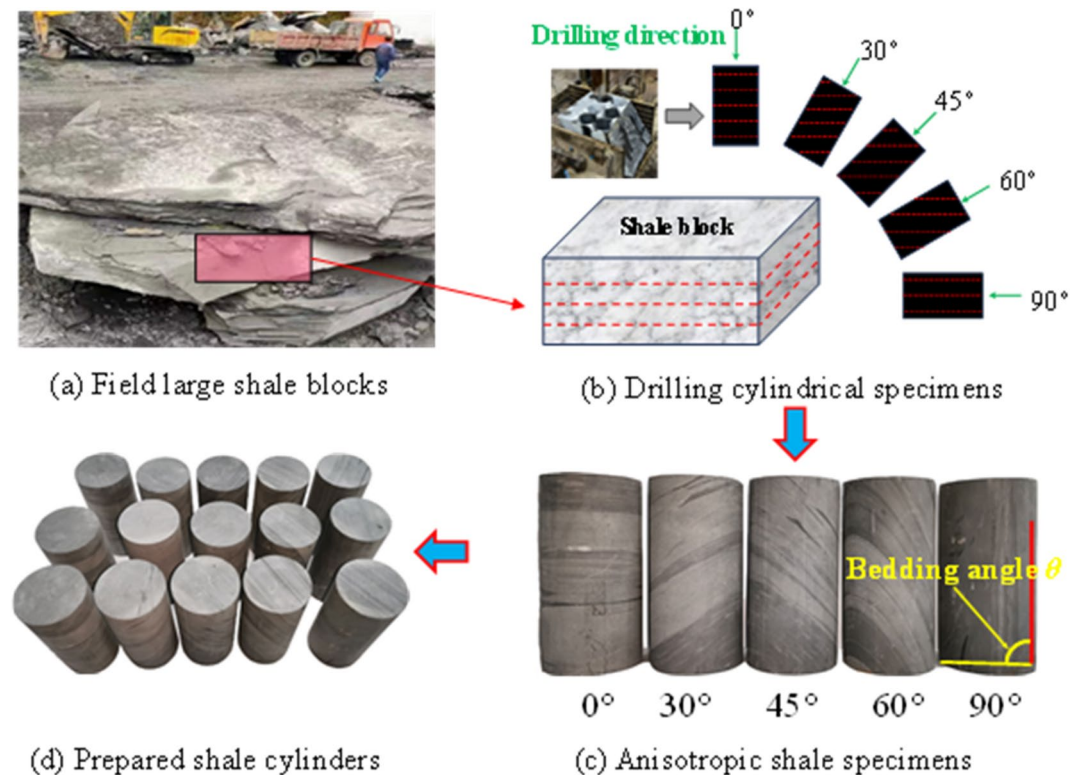


**Fig. 1.** Shale sampling and preparation process.

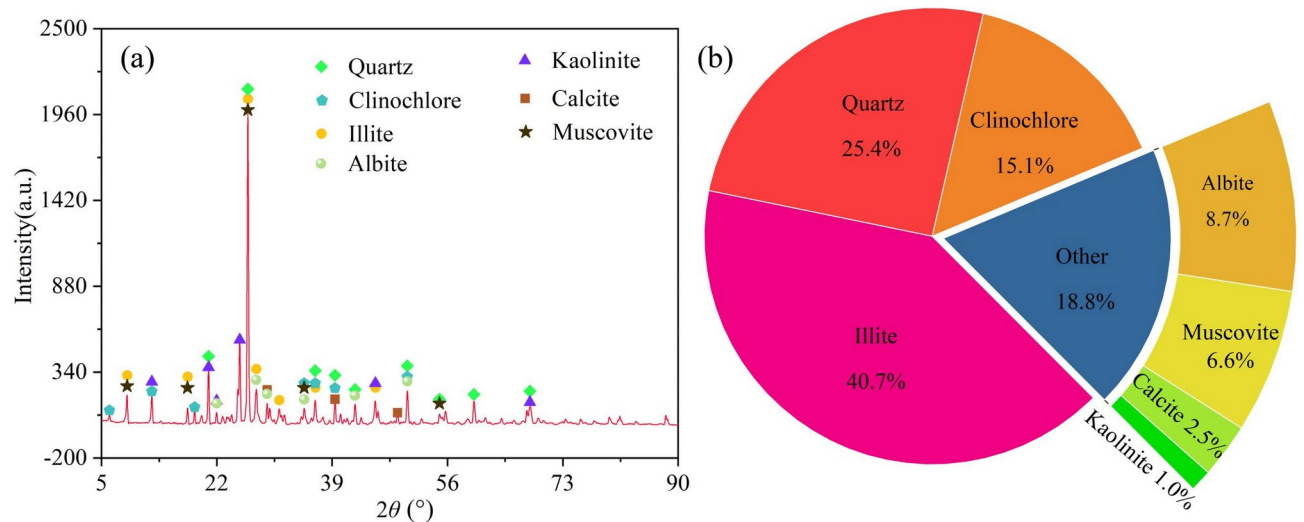


**Fig. 2.** Analysis of mineral composition of Lushan shale: (a) X-ray diffraction of different minerals, and (b) mineral composition content.



**Fig. 3.** WSD4-shaped wave velocity testers.

- (1) Sample preparation: A total of 15 samples are processed and numbered, with three samples prepared for each bedding angle of 0°, 30°, 45°, 60° and 90°, respectively.
- (2) AE sensor fixing: Two AE sensors are fastened on the surface of the specimen by black insulating tape (see Fig. 4). To ensure continuous acquisition of AE signals, Vaseline is applied to the contact surface between the specimen and the AE sensors. And pencil lead break tests are conducted to evaluate acoustic coupling effects.
- (3) Loading: A preloading stress of 0.1 MPa load is applied to the specimen to ensure effective contact between the gasket of the testing machine and the rock specimen. Then, the axial loads are applied to the specimen at a constant rate of 0.1 mm/min until the rock specimen is fractured.
- (4) Post-fracturing observation: Macroscopic inspection of the failure specimen via a digital camera and a microscope is performed to characterize the morphological characteristics of the induced cracks.

### AE data processing

#### Rising angle (RA)-average frequency (AF)

Micro-cracks in engineering structures under test can propagate during rock deformation process, resulting in rapid release of strain energy and AE signals<sup>33</sup>. In other words, AE signals are closely related to the closure,

No.	Height (H) (mm)	Diameter (Φ) (mm)	Density(ρ) (g/cm <sup>3</sup> )	Longitudinal wave velocity (km/s)
0°-1	100.31	50.15	2.612	5.32
0°-2	100.03	50.18	2.621	5.35
0°-3	99.92	49.94	2.611	5.32
Mean value	100.07	49.96	2.609	5.29
30°-1	99.86	50.25	2.623	5.29
30°-2	100.13	50.06	2.611	5.22
30°-3	100.22	49.97	2.632	5.25
Mean value	100.16	50.25	2.624	5.25
45°-1	99.97	50.02	2.650	5.18
45°-2	99.95	50.21	2.631	5.16
45°-3	100.08	50.09	2.627	5.15
Mean value	99.99	50.17	2.637	5.17
60°-1	99.93	50.12	2.589	5.81
60°-2	99.89	50.06	2.602	5.75
60°-3	100.06	49.91	2.596	5.77
Mean value	100.08	49.83	2.596	5.74
90°-1	99.87	49.93	2.603	6.19
90°-2	100.05	50.22	2.615	6.10
90°-3	100.16	50.01	2.611	6.07
Mean value	100.19	50.21	2.633	6.13

**Table 1.** Basic parameters of shale specimens.

initiation, extension and coalescence of micro-cracks as well as the cracking intensity and failure patterns<sup>34</sup>. Stretch mode (mode I) events involve opposite movements on the cracking side, resulting in shorter rise times and higher frequencies for AE waveforms. However, shear mode (mode II) events involve plane sliding on the crack side, resulting in longer rise times and lower frequencies of the acoustic emission waveform<sup>35</sup>. The above fracture mechanism can be elucidated by the relationship between rising angle and average frequency (hereinafter referred to as RA-AF), as shown in Fig. 5. These two key AE parameters can be calculated using

$$RA = \frac{RT}{A} \quad (1)$$

$$AF = \frac{AC}{D} \quad (2)$$

where RA represents the rising angle (ms/v), RT represents the rise time (μs), AF represents the average frequency (kHz), AC represents the AE count, D represents the duration (μs), and A represents the peak amplitude (dB). To standardize the units of AE parameters, Eq. (1) should be converted to<sup>35</sup>

$$RA = \frac{RT}{10^{\frac{A}{20}-1}} \quad (3)$$

The dividing line in the RA-AF value distribution plot is defined as  $k$  ( $k = \text{maximum ordinate value}/\text{maximum abscissa value}$ ). In case of  $AF/RA > k$ , the crack failure is tensile failure; for  $AF/RA < k$ , crack failure is in the form of shear failure.

#### AE amplitude (*b*-value)

The dynamic characterization of the AE *b*-value (hereinafter referred to as *b*-value) reflects the distribution characteristics of the micro-fractures size within the rock during loading. The *b*-value originates from the Gutenberg Richter (G-R) relationship in seismology. That is, the logarithm of the cumulative number  $N$  of a regional earthquake greater than  $M$  magnitude, which has a linear relationship with  $M$ , as given by

$$\text{Log}N = a - bM \quad (4)$$

where  $a$  and  $b$  are constants that represent earthquake activity and the proportional relationship among small and large earthquakes, both results are obtained through data fitting. And  $N$  is the total number of the events with the earthquake magnitude exceeding  $M$ . When analyzing AE parameters, the earthquake magnitude can usually be replaced by the AE amplitude divided by 20, (i.e.  $M = A/20$ ) to eliminate the error in the conversion from Bells to dB<sup>36</sup>. Then, the acoustic emission *b*-value obtained by Eq. (4) can be rewritten as

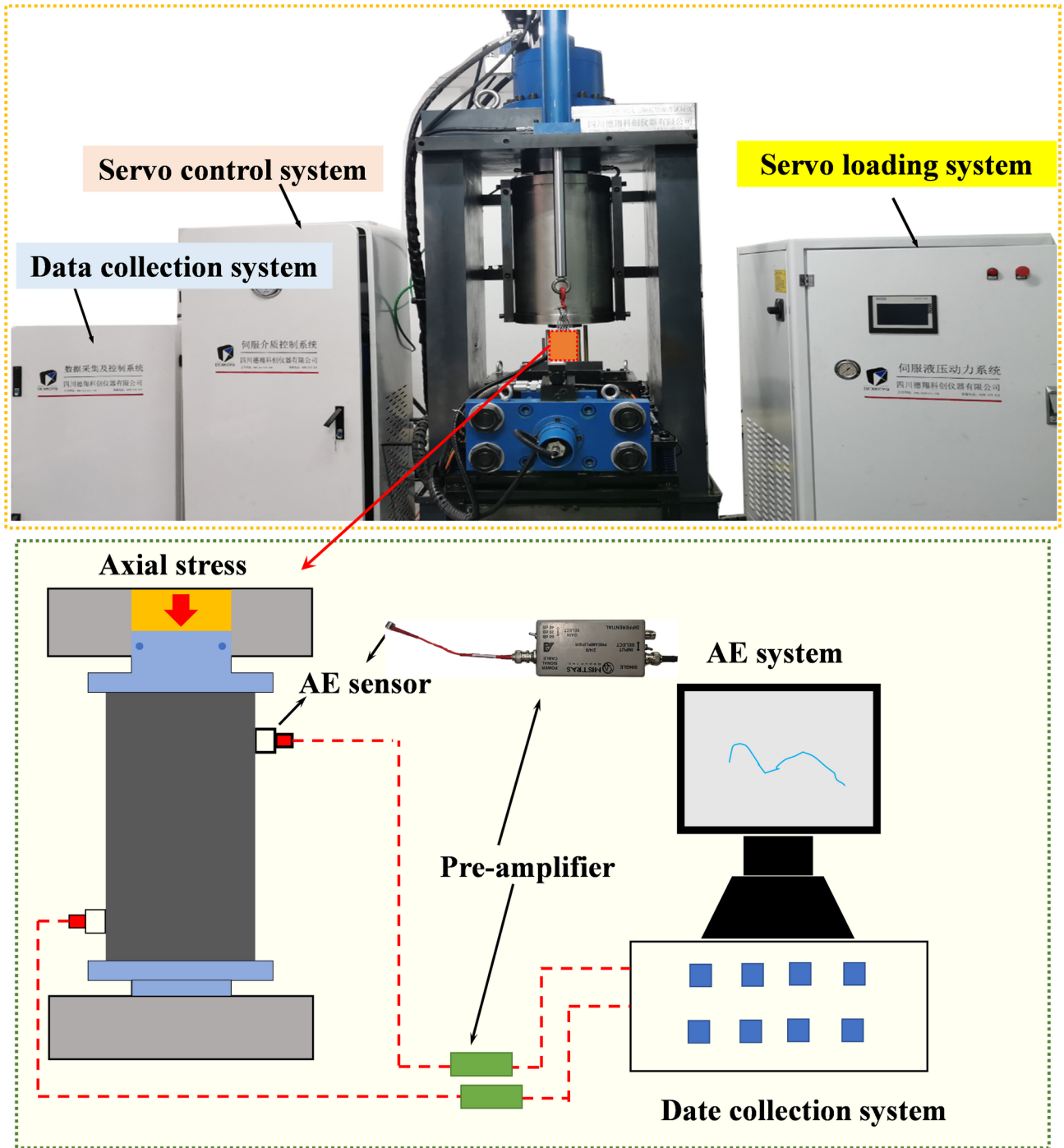


Fig. 4. Experimental equipment diagrams.

$$b = \frac{20 (a - \log N)}{A} \tag{5}$$

The parameter *b*-value demonstrates the proportion of small to large seismic events, which can reflect the scale distribution of AE events and be used for the precursor analysis and prediction of rock failure<sup>37</sup>. A higher *b*-value usually signifies a dominance of smaller-magnitude microcracks, whereas a sharp decline in the *b*-value suggests an increase in larger-scale cracking events, which often precedes macroscopic failure<sup>38</sup>.

#### Fractal dimension of AE counts

The AE signals of rock process failure contain a large amount of information, which provides an effective and reliable method for understanding the physical properties and mechanical instability of rocks<sup>39</sup>. Grassberger

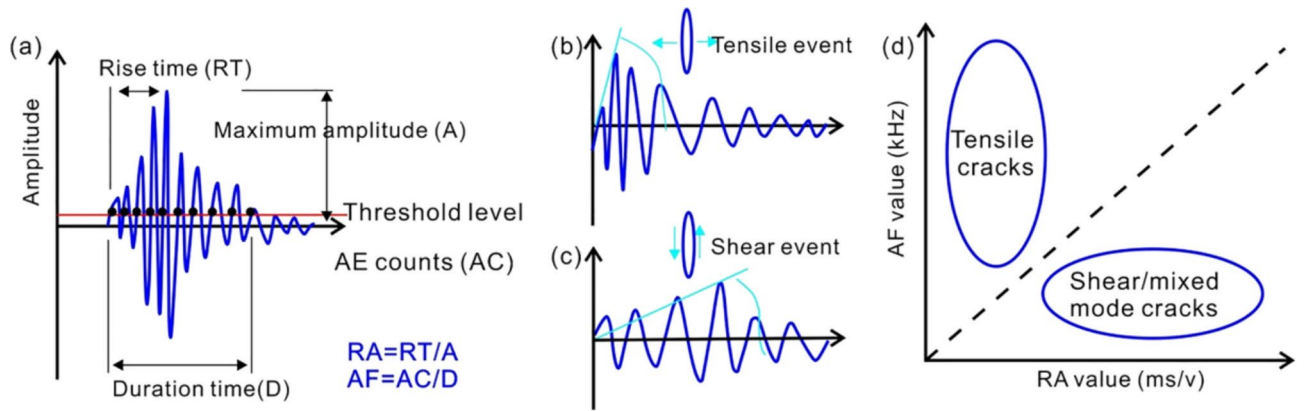


**Fig. 5.** Definition of acoustic emission parameters and crack classification method<sup>33</sup>.

and Procaccia proposed the G-P algorithm in 1983<sup>40–42</sup>. According to the algorithm, the AE sequence needs to form an  $m$ -dimensional phase space, and the phase space is reconstructed by using the time difference<sup>43</sup>, and a series of vector  $X$  with capacity  $n$  based on the AE parameters can be obtained based on the of AE counts, as shown in Eq. (6):

$$X = x_1, x_2, \dots, x_n \tag{6}$$

where  $n$  is the dimension of the reconstructed phase space, and  $X$  is the vector of the reconstructed phase space. So the first vector is:

$$X_1 = x_1, x_2, \dots, x_n \tag{7}$$

After moving  $m$  digits, the  $N$ -th ( $N = n - m + 1$ ) vector, can be expressed by

$$X_N = x_{n-m+1}, x_{n-m+2}, \dots, x_n \tag{8}$$

Through phase space reconstruction, the correlation dimension  $W(r)$  can be calculated by

$$W(r) = \frac{1}{N^2} \cdot \sum_{i=1}^N \sum_{j=1}^N H[r - |X_i - X_j|] \tag{9}$$

where  $H(u)$  is the Heaviside function with the expression of

$$H(u) = \begin{cases} 0, & u < 0 \\ 1, & u \geq 0 \end{cases} \tag{10}$$

and  $r$  is the given scaling function. To avoid discreteness, its expression is as follows:

$$r = k_{sf} r_0 \tag{11}$$

$$r_0 = \frac{1}{N^2} \cdot \sum_{i=1}^N \sum_{j=1}^N |X_i - X_j| \tag{12}$$

where  $k_{sf}$  is the scaling factor, the values in this paper are 0.2, 0.4, 0.6, 0.8, 1.0, 1.2, and 1.4, because when  $k_{sf} \leq 0.1$ , the fractal feature of AE is not obvious<sup>44</sup>.

For a given  $r$ , there is a corresponding correlation function  $W(r)$ . The points ( $\lg r, \lg W(r)$ ) are plotted and fitted in double logarithmic coordinates. If the result of the fit is a straight line, it means that the AE series has a fractal feature in that scale range, and the correlation dimension  $D_{AE}$  is the slope of the straight line, and the expression is as follows:

$$D_{AE} = \lg W(r) / \lg r \tag{13}$$

### Fractal statistics of shale segments

The fractal dimension quantitatively characterizes the irregularity and roughness of fracture fragments and help understand the damage degree of rock sample<sup>45–49</sup>. For these reasons, the fractal dimension has been extensively employed to describe the complexity of fractured surfaces of rocks and analyze rock fracture patterns. The particle size-quantity method is adopted to determine the fractal dimension of fractured Lushan shale with the expression of<sup>45,48</sup>

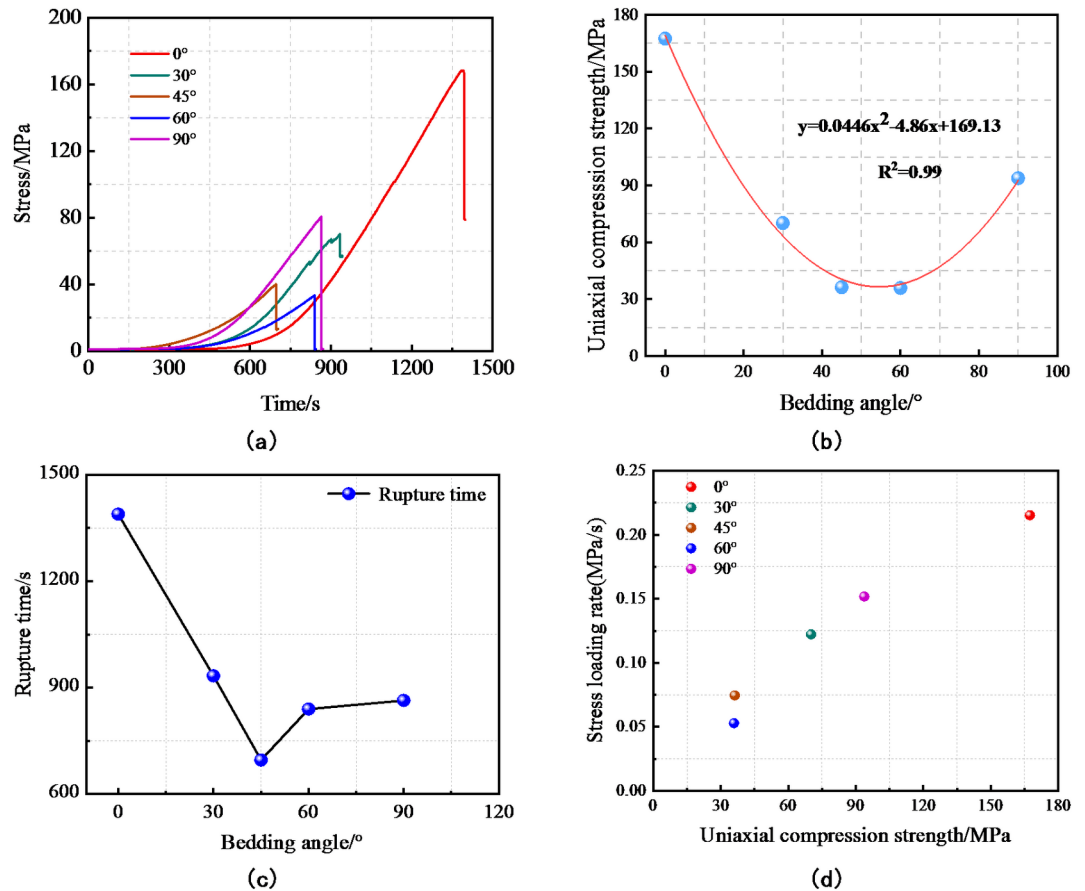


**Fig. 6.** Experimental results of shale under different bedding angles: (a) curves of stress versus time, (b) variation of uniaxial compression strength versus bedding angle, (c) variation of rupture time versus bedding angle, (d) relationship between uniaxial compressive strength and stress loading rate.

Samples No.	$\sigma$ (MPa)	Samples No.	$\sigma$ (MPa)	Samples No.	$\sigma$ (MPa)	Samples No.	$\sigma$ (MPa)	Samples No.	$\sigma$ (MPa)
0°-1	168.169	30°-1	71.485	45°-1	32.584	60°-1	33.332	90°-1	85.597
0°-2	165.080	30°-2	70.137	45°-2	36.145	60°-2	34.524	90°-2	80.538
0°-3	168.954	30°-3	68.858	45°-3	40.052	60°-3	39.746	90°-3	115.325
Average value	167.401	Average value	70.160	Average value	36.260	Average value	35.867	Average value	93.802

**Table 2.** Summary of shale mechanical parameters from uniaxial compression tests.

$$N_f = N_0(L_{eq}/L_{eqmax})^{-D_f} \tag{14}$$

where  $L_{eq}$  is the equivalent side length converted from the square of actual length, width and thickness of rock fragment,  $L_{eqmax}$  is the maximum equivalent side length,  $N_f$  is the number of fragments with equivalent side lengths equal to or greater than  $L_{eq}$ ,  $N_0$  is the number of fragments with the largest feature scale  $L_{eqmax}$ , and  $D_f$  is the fractal dimension.

### Results and analysis

#### Stress–time curves

Figure 6; Table 2 present the results obtained for shale under varying bedding inclinations. When the bedding angle is 0° (Fig. 6a), the average uniaxial compressive strength (UCS) reaches its maximum value of 167.40 MPa. In Fig. 6b, the UCS initially decreases and subsequently increases, with the lowest value of 35.87 MPa observed at a bedding angle of 60°. At the bedding angle of 90°, the average uniaxial compressive strength attains a value of 93.82 MPa. The relationship between uniaxial compressive strength and bedding inclination generally adheres to a polynomial correlation, exhibiting a fitting accuracy of 0.99, as expressed by

$$\sigma = 0.0446\theta^2 - 4.8641\theta + 169.13 \tag{15}$$

where  $\sigma$  is the average UCS, and  $\theta$  is the bedding angle. This implies that the bedding angle of the rock sample has a significant influence on the peak strength of shale<sup>50,51</sup>. According to Eq. (15), it can be inferred that the UCS has the minimum value at  $\theta = 54.53^\circ$ , which is about 36.51 MPa. Hence, when undertaking fracturing operations and extracting shale gas from Lushan shale formations, it is imperative to comprehensively consider the impact of bedding angle on the mechanical properties, as this can significantly influence the formation breakdown strength and the outcome of the extraction process<sup>52</sup>.

As shown in Fig. 6c, the rupture time (i.e., the loading time when the maximum stress is measured) decreases and then increases with increasing bedding angles, which is consistent with the tendency of UCS variation in Fig. 6b. It is worth noting that the rupture time at the bedding angle of  $90^\circ$  is shorter than that of the  $30^\circ$ , which may be due to the influence of pre-existing cracks or joints inside the specimen<sup>53–55</sup>. As can be seen from Fig. 6b and c, at bedding angles of  $\theta = 45^\circ$  and  $\theta = 60^\circ$ , the uniaxial compressive strength remains almost identical. However, the rupture time at  $\theta = 60^\circ$  is notably longer than that at  $\theta = 45^\circ$ . This disparity can be attributed to the existence of natural microcracks within the specimen, which lead to variations in the crack propagation velocities during the loading process<sup>56–58</sup>. To gain a deeper understanding of stress variations across varying bedding inclinations, we have introduced the concept of a stress loading rate (linear fitting of the stress curve, the resulting slope is the stress loading rate), which quantifies the rate of stress increase as the load progresses from 50 to 80% of the rock's ultimate strength. As shown in Fig. 6d, the stress loading rate exhibits a positive correlation with the uniaxial compressive strength. The stress loading rate can be divided into three stages: (1) When the uniaxial compressive strength is less than 50 MPa, the stress loading rate is less than 0.1; (2) When the uniaxial compressive strength is between 50 MPa–100 MPa, the stress loading rate is between 0.1 and 0.2; (3) When the uniaxial compressive strength is greater than 100 MPa, the stress loading rate is greater than 0.2. The results show that the uniaxial compressive strength increases with the increase of stress loading rate.

## AE response subjected to uniaxial compression

### AE parameter analysis

The compression failure of brittle rock is mainly divided into five stages: compaction stage (I), elastic deformation stage (II), crack stable propagation stage (III), crack unstable propagation stage (IV) and post-peak failure stage (V), each of which shows evident AE characteristics<sup>59</sup>. Figure 7a–e depict the progression of Acoustic Emission (AE) count and cumulative AE counts across various bedding angles. During Stage I, the rock undergoes a process of compaction and pore closure as axial stress gradually increases, prior to entering the linear elastic stage. This initial phase generates a relatively small number of AE counts. In stage II, the steady increase in AE counts indicates the continuous expansion of pre-existing microfractures within the shale, as well as the initiation of new fractures. However, the rate of increase in AE count remains relatively modest, manifesting as a nearly linear trend of escalation. During Stage III, the AE counts rise linearly, signifying the emergence of new cracks or the full development of existing natural cracks. In Stage IV, there is a marked surge in AE count, indicative of locally initiated cracks beginning to coalesce and interconnect with each other. The instantaneous failure of the rock results in an abrupt drop in axial stress, accompanied by a simultaneous, sharp decrease in the cumulative AE counts. Comparing Fig. 7a–e, it is evident that there exists a strong correlation between the variations in AE counts, cumulative AE counts, and stress values across different bedding angles. To gain further insights into the differences in fracture evolution at various bedding angles, Fig. 7f presents a comparative plot of cumulative AE counts for different samples. It is apparent that a higher uniaxial compression strength is associated with larger cumulative AE counts. However, an interesting observation is that for a bedding angle of  $\theta = 45^\circ$ , the cumulative AE counts are lower than that observed for  $\theta = 60^\circ$ . This could be attributed to the reduced bedding inclination with respect to the axial load at steeper bedding angle that facilitates the failure of shale during loading<sup>60</sup>.

Figure 8a shows the comparison of UCS and the peak AE count at different bedding angles  $\theta$ . For a bedding angle of  $\theta = 0^\circ$ , the corresponding peak AE count is the highest, which coincides with the largest UCS observed. When the bedding angles are  $\theta = 45^\circ$  and  $\theta = 60^\circ$ , the UCSs are nearly identical. However, the peak AE count at  $\theta = 60^\circ$  is greater than that at  $\theta = 45^\circ$ , which can potentially be attributed to the influence of naturally occurring cracks within the rock during its compressive failure<sup>60</sup>. When  $\theta = 30^\circ$ , the UCS and peak AE count are in the middle position. The greater UCS seems always corresponds to larger peak AE count. Figure 8b shows the evolution of the peak AE count and cumulative AE counts versus bedding angle  $\theta$ . It is evident that as the bedding angle increases, the peak AE count follows distinct a “V” shaped pattern. It can be seen from Fig. 8b that the peak AE count decreases gradually between  $\theta = 0^\circ \sim 45^\circ$ , consistent with the variation of uniaxial compressive strength in Fig. 6b. When the bedding angle ranges from  $\theta = 45^\circ$  to  $90^\circ$ , both the uniaxial compressive strength and the peak AE count begin to exhibit an increasing trend. (see Figs. 6b and 8b). As the bedding angle  $\theta$  increases, the cumulative AE counts exhibit an “M” shaped pattern. Notably, at  $\theta = 30^\circ$ , the cumulative AE counts reach its maximum, despite the relatively low UCS observed in Fig. 6b. A plausible explanation for this phenomenon could be the presence of numerous micro-cracks within the rock sample, which may propagate and coalesce with each other, leading to the generation of continuous and dense AE signals upon the occurrence of shale failure<sup>61,62</sup>.

### AE *b*-value

As previously stated, the dynamic evolution of the *b*-value provides insights into the distribution characteristics of micro-fracture scales within the rock during the loading process. The mutation of *b*-value is also one of the important precursors for rock failure. Figure 9 shows the evolution of *b*-value and axial stress during loading process. During the initial loading stage, the *b*-value undergoes minor fluctuations, suggesting that the proportion of large and small AE events remains relatively stable and unchanged. This indicates that the expansion of microcracks at various scales remains relatively stable during this initial period. However, as the stress increases, the *b*-value commences to rise, signifying an increasing proportion of micro-cracks within

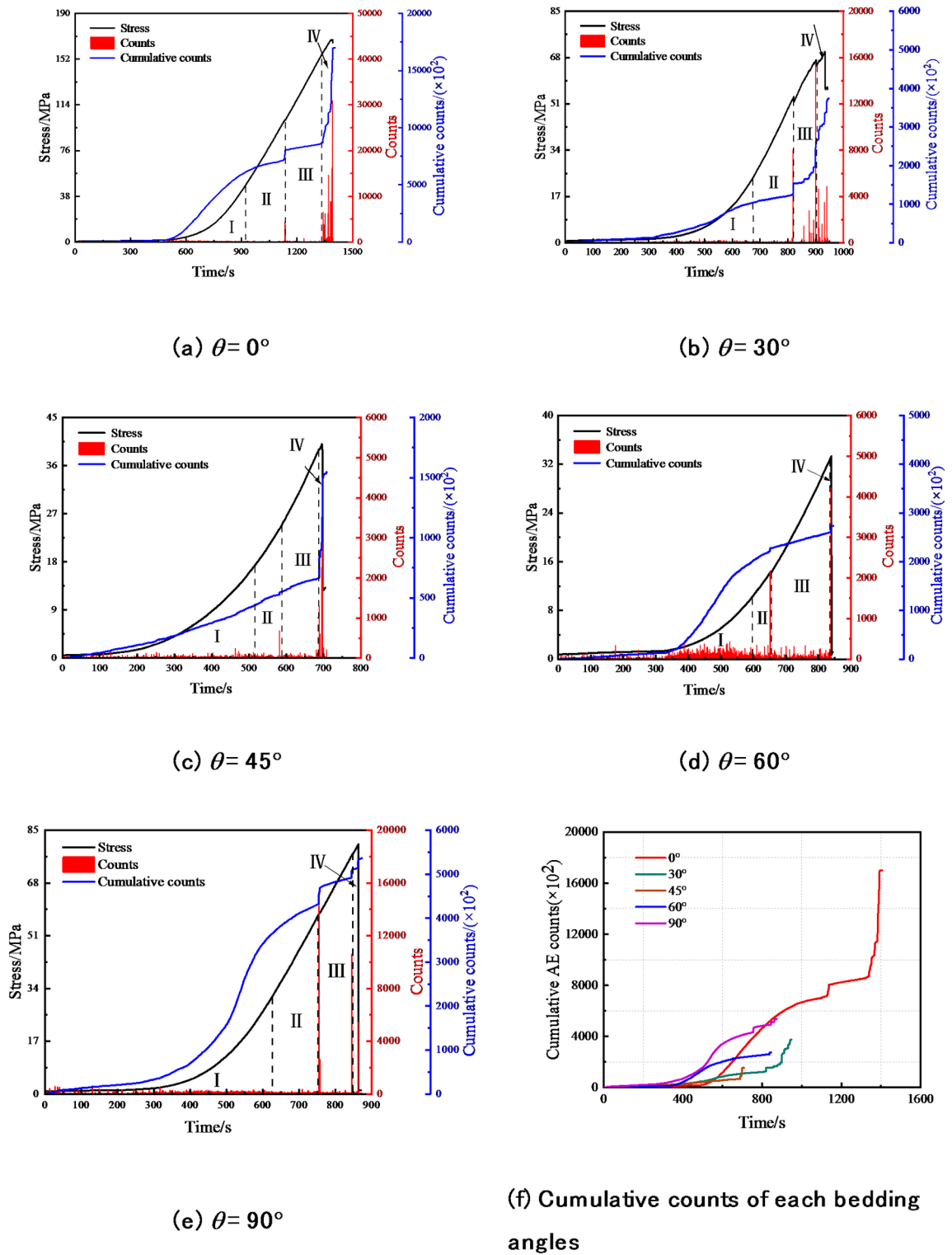
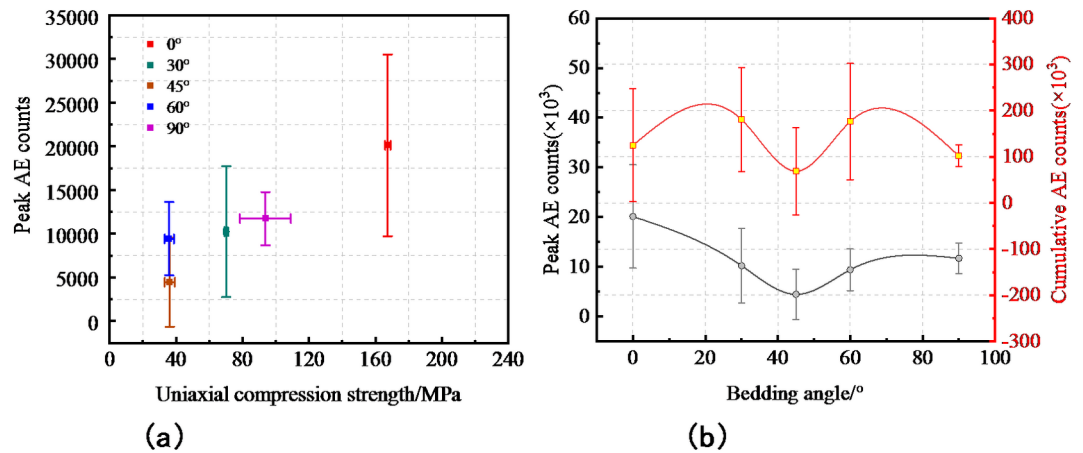


Fig. 7. AE count and cumulative AE counts evolution curves under different bedding angles.

the rock. Upon reaching 70% ~ 80% of the peak stress, the  $b$ -value exhibits a sudden drop. The decrease in the  $b$ -value signifies a shift towards a higher proportion of high-magnitude AE events, indicating instability as small-scale microfractures coalesce into larger-scale cracks. Irrespective of different bedding angles, the change trend of the  $b$ -value is roughly the same, and the  $b$ -value at peak stress is always lower than that during the stress loading stage. Figure 9f shows the peak  $b$ -value of shale specimens at different bedding angles. The peak  $b$ -value for the shale samples across various bedding angles hovered around 2.0, with the exception of the  $30^\circ$  bedding angle, which displayed a  $b$ -value of approximately 1.5. This divergence in  $b$ -value may be attributed to



**Fig. 8.** Analysis of AE count and cumulative AE counts diagram: (a) Relationship between uniaxial compression strength and peak AE counts; (b) Relationship between layer inclination angle and peak AE counts/cumulative AE counts.

variations in the internal microstructure and porosity of the individual specimens, which potentially disrupted the transmission of AE signals<sup>63</sup>.

### Rising angle-average frequency

The fracture mode of microcracks within rock during loading principally involves two types: tensile fracture and shear fracture<sup>64–67</sup>. Laboratory experiments involving AE monitoring typically reveal that shear waves exhibit relatively low AF values and high RA values, whereas tensile failure is distinguished by relatively high AF values and low RA values<sup>68</sup>.

As depicted in Fig. 10a, the range of RA distribution for shale samples with  $\theta=0^\circ$  is predominantly centered within 10 to 40 ms/V, while the distribution of AF values is largely confined to 50 to 350 kHz. This comprehensive RA-AF value distribution suggests that the primary mode of failure for samples featuring a horizontal bedding angle is tensile in nature. From Fig. 10b, we see that the distribution ranges of RA-AF values of shale specimen with  $\theta=30^\circ$  are concentrated in 9 to 30 ms/V and 100 to 300 kHz, respectively. In Fig. 10c, the RA value of the shale specimen with  $\theta=45^\circ$  is predominantly concentrated within the range of 6 to 20 ms/V, while the AF value distribution spans from 50 to 200 kHz. This observation signifies a notable decrease in the RA-AF value signal. In Fig. 10d, the RA value of the shale specimen with  $\theta=60^\circ$  is clustered primarily within the range of 7 to 12 ms/V, while the AF value is concentrated between 70 and 170 kHz. Notably, the overall RA-AF value for this sample is lower in comparison to the other specimens. As for Fig. 10e, the RA value of the shale specimen with  $\theta=90^\circ$  is predominantly concentrated within the range of 5 to 15 ms/V, while the AF value spans from 75 to 250 kHz. Notably, there is a significant increase in the RA value signal, however, this sample with a bedding angle of  $90^\circ$  primarily exhibits characteristics of tensile fracture.

According to the evolution of different types of cracks, we can divide the loading process into three stages. During Stage I, the tensile fracture undergoes an ascending phase, whereas the shear fracture progresses through a descending phase. In Stage II, the relative proportions of tensile fracture and shear fracture remain relatively stable and consistent. During Stage III, the tensile fracture transitions into a descending phase, while the shear fracture enters an ascending phase. Within 750 ~ 1350s of  $\theta=0^\circ$ , the proportion of cracks of the two types is almost unchanged. Within 750 ~ 900s of  $\theta=30^\circ$ , the shear crack increases and the tensile crack decreases. Within 300 ~ 600s at  $\theta=45^\circ$ , the shear cracks also increase. Approximately at 700s and at  $\theta=60^\circ$ , the proportion of tensile cracks attains its peak. The proportion of shear cracks at  $\theta=90^\circ$  has a sudden decline at about 700s. The fluctuations in the proportions of tensile and shear cracks can potentially be attributed to variations in the bedding angle, which subsequently lead to alterations in stress redistribution. Shales exhibiting varying bedding angles possess distinct strength and fracture characteristics. Consequently, the uneven stress distribution encountered during loading results in continuous alterations in the proportions of the two types of cracks. It is worth noting that at  $\theta=30^\circ$ , no shear cracks occur during the first five phases.

In summary, the uniaxial compression failure of shale with diverse bedding angles is predominantly influenced by the process of tensile cracking. More specifically, when the bedding angle is less than  $45^\circ$ , the failure of shale is predominantly governed by tensile cracks, with shear cracks contributing to less than 10% of the overall failure mechanism. When the bedding angle equals or surpasses  $45^\circ$ , there is a notable increase in the proportion of shear cracks, particularly pronounced at a bedding angle of  $90^\circ$ . It is noteworthy that the relatively low RA-AF values observed at bedding angles of  $45^\circ$  and  $90^\circ$  suggest that shale samples at these orientations possess a comparatively reduced proportion of tensile cracks. In contrast, relatively abundant shear cracks are observed at these angles. The prevalence of shear cracks indicates that substantial shear stress components are generated on the shale layer surfaces when the angle between the stress direction and the bedding plane approaches  $45^\circ$  or  $0^\circ$ , leading to the prolific formation of shear cracks.

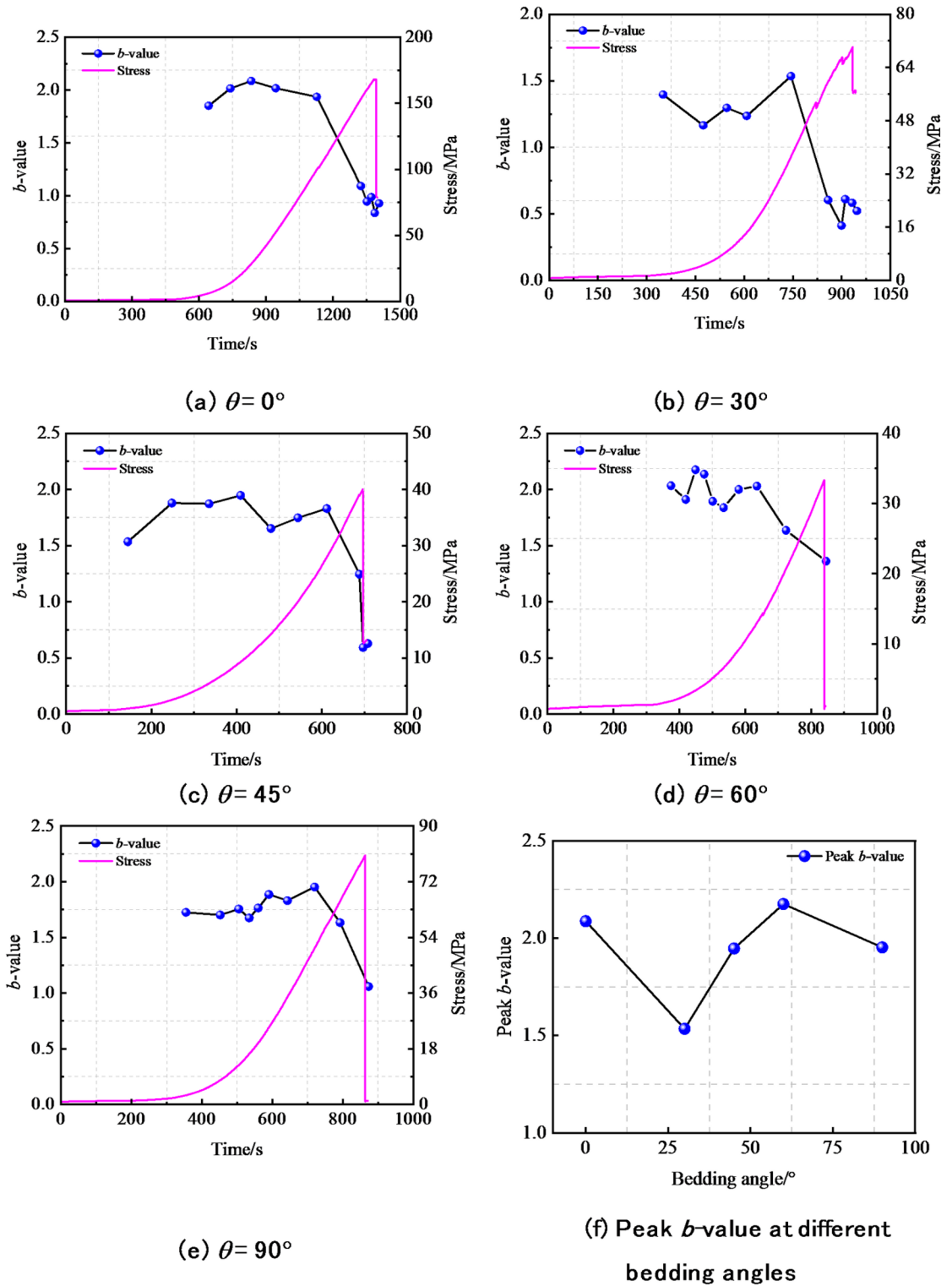
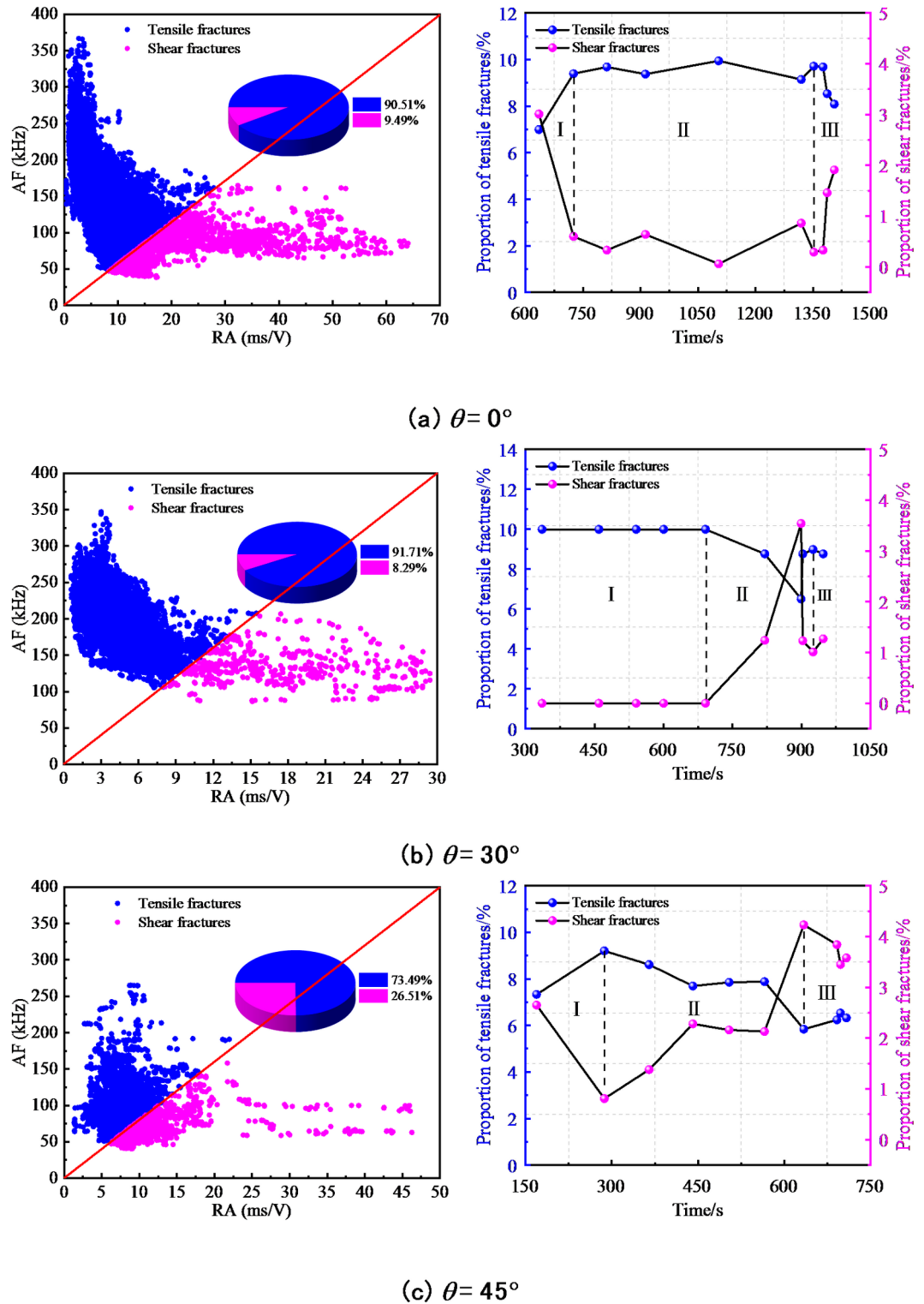


Fig. 9. Evolution of  $b$ -value and axial stress under different bedding angles.

### Fractal characteristics of AE parameters

For clarity, we take  $\theta = 0^\circ$  and  $\theta = 90^\circ$  as examples to analyze the evolution of correlation dimension. As shown in Fig. 11, the variation trend of the correlation dimension  $D_{AE}$  for shale with varying bedding angles generally follows a similar pattern, aligning with the change trend observed in the correlation dimension  $D_{AE}$  of shale with different bedding angles under Brazilian splitting<sup>44</sup>. The dynamic change process can also be divided into four parts according to the stress-time curve shown in Fig. 7. The initial phase is the compaction stage (I), during which the AE signals primarily originate from the compaction of primary pores and inherent microcracks. As



**Fig. 10.** Classification of crack modes in 45° straight line under uniaxial compression test and evolution of fractures during loading.

shown in Fig. 11, during this stage, the correlation dimension remains relatively unchanged, exhibiting a flat trend. This may be associated with the stable evolution of AE counts as previously revealed in Fig. 7. The second phase (II) corresponds to the elastic stage, where microcracks commence to form within the specimen, leading to a slight fluctuation in the evolution trend of the correlation dimension  $D_{AE}$ . The third phase (III) represents the crack stable expansion stage, where the microcracks within the specimen propagate and coalesce to form macroscopic cracks, accompanied by a surge in AE counts. The fourth phase (IV) marks the onset of rock failure,

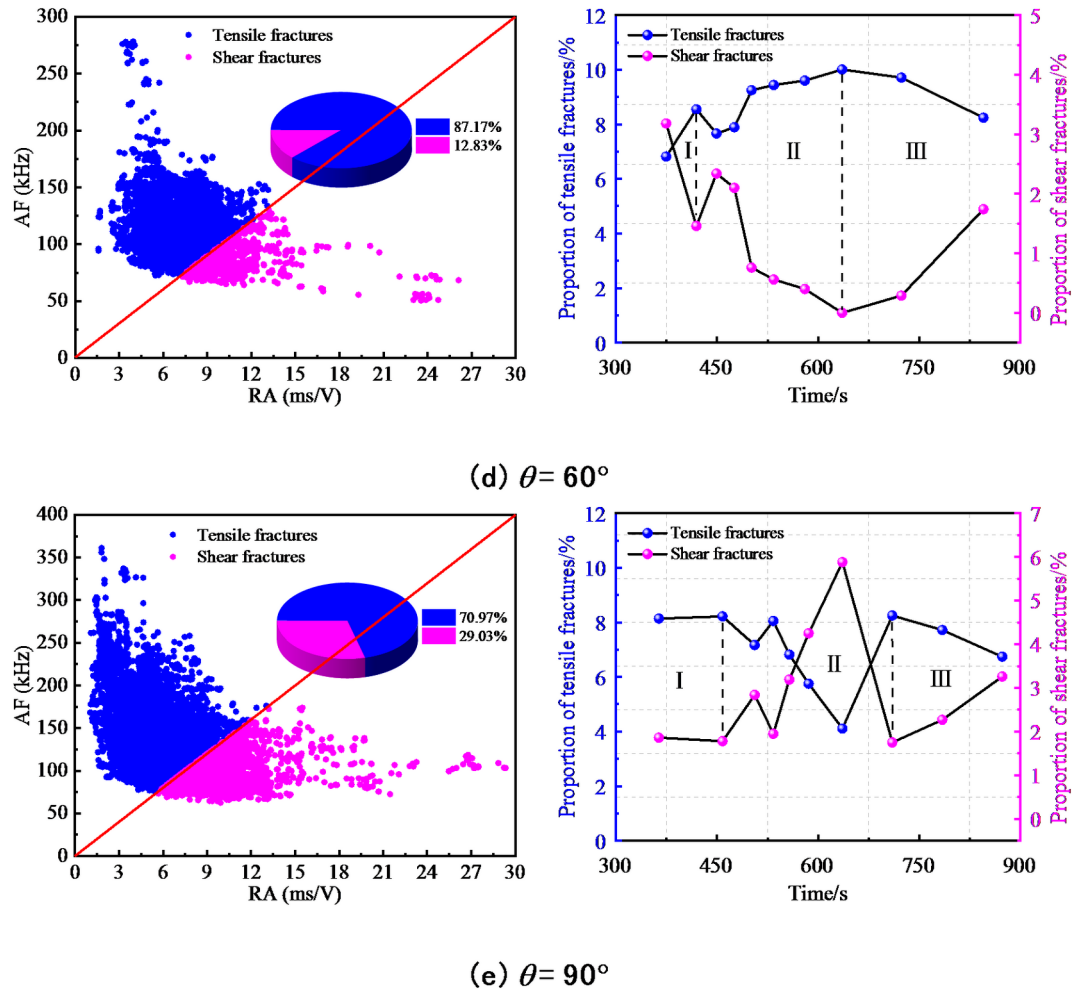


Fig. 10. (continued)

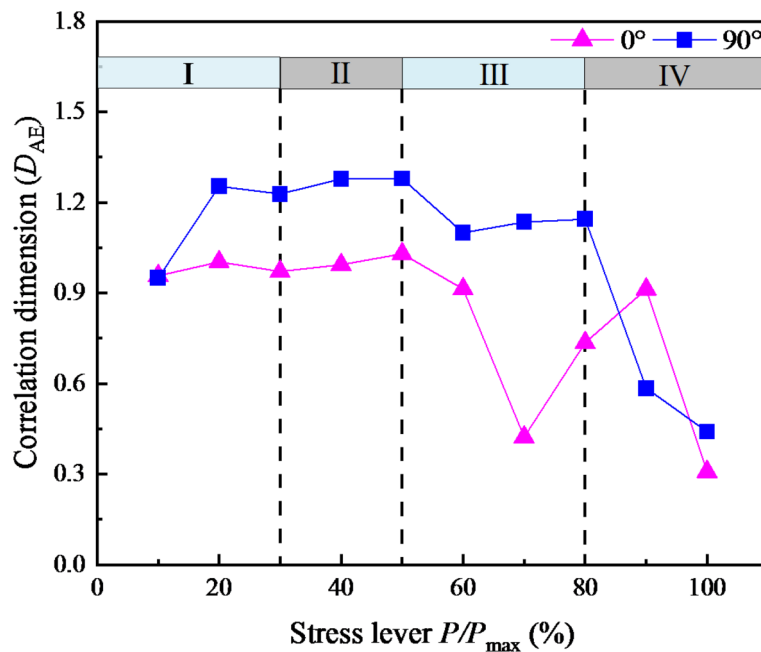


Fig. 11. Fractal dimension of AE at different stress stages.

characterized by the generation of a significant number of microcracks during the macroscopic failure process. As a result, the correlation dimension  $D_{AE}$  decreases sharply and continuously, with a smallest value appeared at the peak stress ( $100\%P/P_{max}$ .)

Moreover, it is evident that, regardless of the specific bedding angle, the correlation dimension  $D_{AE}$  generally exhibits a decreasing trend once the stress reaches 80% of the peak stress. This phenomenon can be attributed to the coalescence of microcracks during the fracture development stage (III), which leads to a reduction in the number of microcracks and consequently, a decrease in the fractal dimension of AE events. However, an interesting observation is that when  $\theta$  equals  $0^\circ$ , there is a slight increase in the correlation dimension, which notably contrasts with the continuous decreasing trend observed in the correlation dimension  $D_{AE}$  for  $\theta=0^\circ$ . We ascribe this phenomenon to the varying bedding angles. In the case of  $\theta=90^\circ$ , the loading direction is aligned with the bedding plane, causing the induced cracks to propagate preferentially along the loading (or bedding) direction. Therefore, there are fewer secondary crack initiations, leading to a consistent decrease in AE events and subsequently, a reduction in the correlation dimension. However, in a bedding-parallel case ( $\theta=90^\circ$ ), the loading is applied perpendicular to the bedding, which may induce new crack initiation even if the stress reaches the peak strength. This results in an increase in AE events, thereby enhancing the fractal characteristics of AE counts.

## Failure pattern

### *Macroscopic failure pattern*

The failure modes of shale include through-bedding failure, through-bedding shear-slip failure, layer-slip failure, slip-shear failure and radial tension failure when the bedding angles  $\theta$  ranges from  $0^\circ$  to  $90^\circ$ . In Fig. 12, a representative specimen from each bedding angle, which underwent failure during uniaxial compression loading, was carefully selected and subjected to detailed analysis. At a bedding angle of  $\theta=0^\circ$ , the specimen's surface displays a complex pattern of intersecting cracks, featuring seven distinct secondary cracks aligned along the layer. The tensile failure is evident, and the failure mode is through-layer fracture failure. When  $\theta$  equals  $30^\circ$ , a subtle caving is evident at the upper extremity of the specimen, accompanied by numerous transverse secondary cracks on its surface, indicative of layer-slip failure. At  $\theta=45^\circ$ , spalling is observed both at the upper and lower ends of the specimen, with two vertical splitting cracks forming a distinct "V" shaped failure pattern. The two parallel secondary cracks originate from the upper end of the specimen and converge at the bottom of the specimen, and the failure mode is layer-slip failure with vertical splitting cracks. The specimen remains relatively intact without significant deformation while  $\theta=60^\circ$ . It exhibits a progressive "V"-shaped crack pattern during failure, and numerous small cracks appear on both sides of the "V" cracks, ultimately penetrating the specimen. This failure mode is predominantly characterized by tensile failure, with the primary mechanism involving shear slip along the layers of the specimen, resulting in its disintegration. Furthermore, at  $\theta=90^\circ$ , the specimen experiences more noticeable deformation. Numerous small fragments dislodge from both the ends and sides of the specimen. Furthermore, two distinct shear cracks originate from the upper extremity of the specimen, progressively extending downwards until they converge at the base of the specimen. Additionally, numerous smaller cracks proliferate throughout the failure zone of the specimen, accompanying these primary shear fractures. Despite the occurrence of shear cracks, the primary mode of failure remains dominated by tensile forces. Analogous to the prior scenario, the dominant failure mechanism is distinguished by shear slip occurring along the layers of the specimen.

The macroscopic failure modes of specimens featuring varying bedding angles demonstrate that those with  $\theta=45^\circ$  exhibit layer-slip failure, characterized by vertical splitting cracks, whereas specimens with  $\theta=90^\circ$  undergo tensile splitting failure accompanied by localized shear cracks. The macroscopic examination of specimens with varying bedding angles reveals that those with  $\theta=45^\circ$  and  $\theta=90^\circ$  display distinct failure modes: the former undergoing layer-slip failure marked by vertical splitting cracks, and the latter experiencing tensile splitting failure with localized shear cracks. There are obvious shear cracks in  $\theta=45^\circ$  and  $\theta=90^\circ$ , but the overall failure mode is dominated by tensile cracks. Furthermore, our observations encompass the presence of rock fragments detaching from both the upper and lower extremities of samples with  $\theta=45^\circ$  and  $\theta=90^\circ$ , respectively. Notably, other specimens displayed no discernible shear cracks and were predominantly characterized by axial tensile cracks, accompanied by secondary cracks. In summary, the macroscopic failure fractures observed in specimens with  $\theta=45^\circ$  and  $\theta=90^\circ$  are predominantly governed by shear failure, aligning with the findings interpreted through the RA-AF analysis. This signifies that the RA-AF value method is a viable approach for identifying the failure mode of shale samples exhibiting varying layer orientations.

### Inspection of main fracture surface

As shown in Fig. 13, the cross-sections of fractured shales with different bedding angles are generally increased. In the case of specimens with  $\theta=0^\circ$ , the layer surface is oriented perpendicular to the compression direction. Consequently, shale failure ensues subsequent to the axial propagation of fractures reaching the bedding surface, suggesting the coexistence of both shear and tensile failure mechanisms on the layer surface. For specimens with  $\theta=30^\circ$  and  $\theta=60^\circ$ , the fracture failure surfaces exhibit similar characteristics to the specimen fracture planes, with bedding angles spanning from  $44^\circ$  to  $78^\circ$ . However, in a specimen with  $\theta=30^\circ$ , the specimen is fractured by shear slip in the shale matrix, while in the specimen with  $\theta=60^\circ$ , layer-slip failure is observed. In specimens with  $\theta=45^\circ$ , the shale failure occurs mainly along the strata. Furthermore, the specimen with  $\theta=90^\circ$  displays a gradual increase in thickness from the upper end to the bottom end, which is indicative of a layer-slip failure mode. These findings reveal that, when the bedding angle  $\theta=30^\circ$ , the shale undergoes a layer-slip fracture mode, accompanied by transverse secondary fractures. For shale samples with  $\theta=0^\circ$  and  $\theta=45^\circ$ , failures predominantly occur along the weaker surfaces inherent to the layer structure. In general, the failure mode of

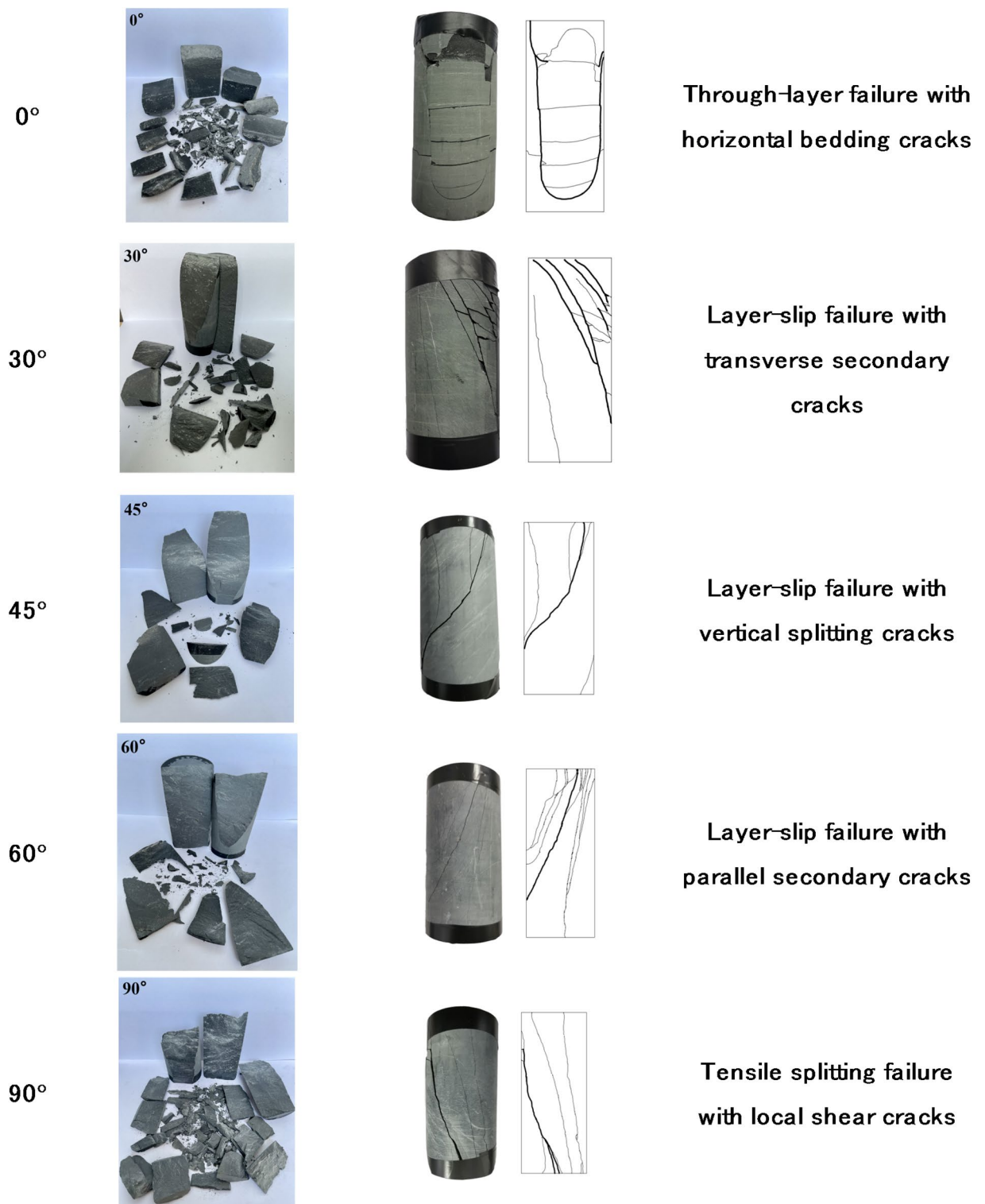


**Fig. 12.** Typical macroscopic failure photos of specimens under uniaxial compression.

shale is intimately tied to its bedding angle. Specifically, shale failures with bedding angles exceeding 45° are predominantly characterized by fractures traversing the bedding planes.

**Fractal characteristics of shale fragments**

Irregular shaped fragments are generated after the uniaxial compression tests. The intensity of energy released increases in proportion to the finer fragmentation of the specimen<sup>48</sup>. Conversely, the larger the fragments generated by the specimen, the lesser is the intensity of energy released. In this section, the fragments were

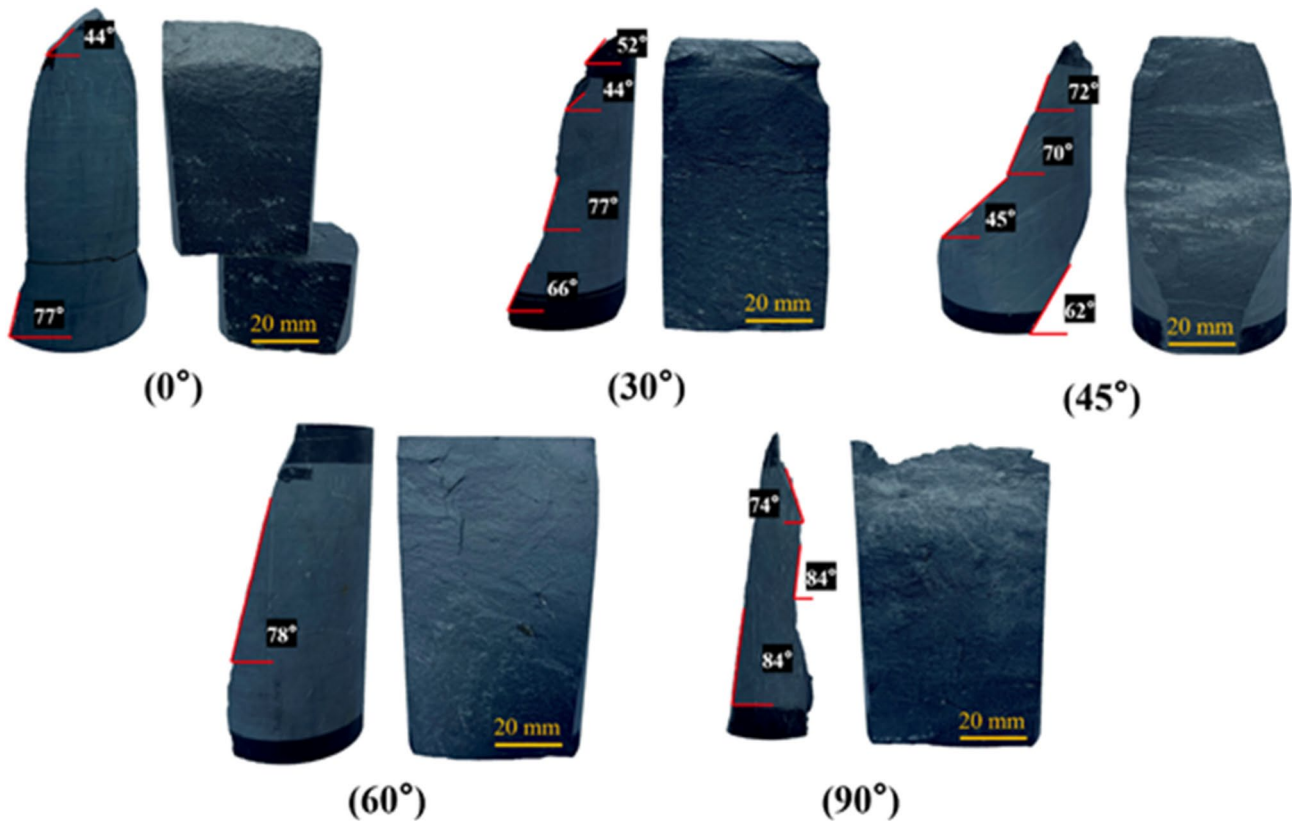


Fig. 13. Shale fracture surfaces with different bedding angles under uniaxial compression.

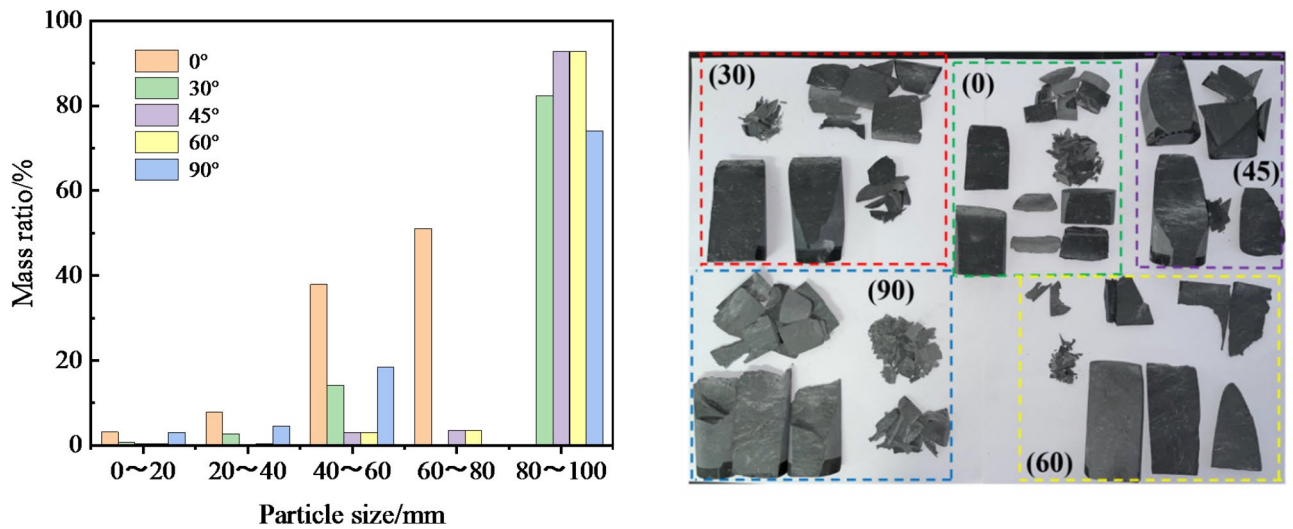


Fig. 14. Fragment classification and mass ratio of different bedding angles.

statistically analyzed in five groups with particle sizes of 0–20 mm, 20–40 mm, 40–60 mm, 60–80 mm and 80–100 mm, as shown in Fig. 14. On an overall basis, the majority of particles, approximately 95%, fall within the size range of 80–100 mm. However, at  $\theta=0^\circ$ , there is no segments within a particle size of 80–100 mm. This is attributed to the through-layer failure mode, which results in the sample being segmented into several smaller pieces, leading to a general reduction in the size of the fractured segments to less than 80 mm. In the case of  $\theta=90^\circ$ , where the stress loading direction is parallel to the layer, a greater number of fragments are produced during the failure process. Consequently, the proportion of segments with a particle size within the 80–100 mm range falls below 90%.

Using the fractal statistical method, the fitting plot of  $\lg(L_{eqmax}/L_{eq})-\lg N$  according to Eq. (6) at different bedding angles is shown in Fig. 15a. Generally, shale fragments at different bedding angles have obvious fractal characteristics. The fractal dimension, ranging from its smallest to largest value, aligns with the  $\theta$  of  $0^\circ$ ,  $90^\circ$ ,  $30^\circ$ ,  $60^\circ$ , and  $45^\circ$ , harmoniously reflecting the geometric attributes, quality and quantity of the categorized fragments as depicted in Fig. 14. Small  $L_{eqmax}/L_{eq}$  corresponds to large fractal dimension ( $D_f$ ). At  $\theta=0^\circ$ ,  $L_{eqmax}$  is up to 66 mm, indicating that the diversity of segments produced during loading failure is abundant, which is related to the failure mode. In other words, the fragments resulting from the through-layer failure mode are not only more numerous but also tend to be smaller in size compared to those generated by alternative failure modes. The  $D_f$  ranges from 1.75 to 3.15, and the fragments generated during the failure process exhibit pronounced variations, indicative of the distinctiveness of the layers within the Lushan shale and a high content of brittle minerals. The  $D_f$  less than 2 indicates that the diversity of larger fragments produced by the specimen during destruction is small.

As shown in Fig. 15b, the trend of fractal dimension under different bedding angles is analyzed. As the bedding angle steadily increases, the overall trend of the  $D_f$  remains in harmony with the uniaxial compressive strength. Notably, at a bedding angle of  $\theta=45^\circ$ , the  $D_f$  exhibits a relatively low value. This can be attributed to the relatively weak bedding planes compared to shale matrix that is easily activated and loss stability when subjected to axial expansion forces. The activation of bedding planes serves to weaken the overall strength of the shale, leading to a less efficient release of energy during the failure process. Consequently, larger segments are produced as a result. Compared with Fig. 7f, the cumulative AE counts for the  $\theta=45^\circ$  is the lowest, corresponding to the smallest fractal dimension. This observation underscores the existence of a correlation between the cumulative AE counts and the calculated  $D_f$ .

### Discussion

#### Impacts of bedding anisotropy on peak strength and AE response

In uniaxial compression tests, the relationship between the uniaxial compressive strength (UCS) and bedding angle ( $\theta$ ) can be explained by the interaction between normal stress and shear stress. The bedding angle determines how the applied compressive force is resolved on the bedding plane, which in turn affects the failure mode and the compressive strength. The compressive stress  $\sigma$  in the loading direction can be decomposed into normal stress  $\sigma_n$  perpendicular to the bedding plane and shear stress  $\tau$  along the bedding plane. Their relationship can be expressed using the following equations:

$$\sigma_n = \sigma \cos^2 \theta \tag{16}$$

$$\tau = \sigma \sin \theta \cos \theta \tag{17}$$

As the bedding angle changes, the ratio between normal stress and shear stress changes significantly, thereby affecting the mechanical behavior of the rock.

To verify the impact of bedding angles on UCS values, we compared our results with those of Niutitang shale sourced from the northwestern Hunan province<sup>69</sup> and Longmaxi shale sourced from Chongqing City<sup>70</sup> in Fig. 16. Irrespective of sampling locations and individual shale formations, the UCS of shale exhibits a consistent trend, initially decreasing and subsequently increasing as the bedding angles increase. In contrast, the Niutitang

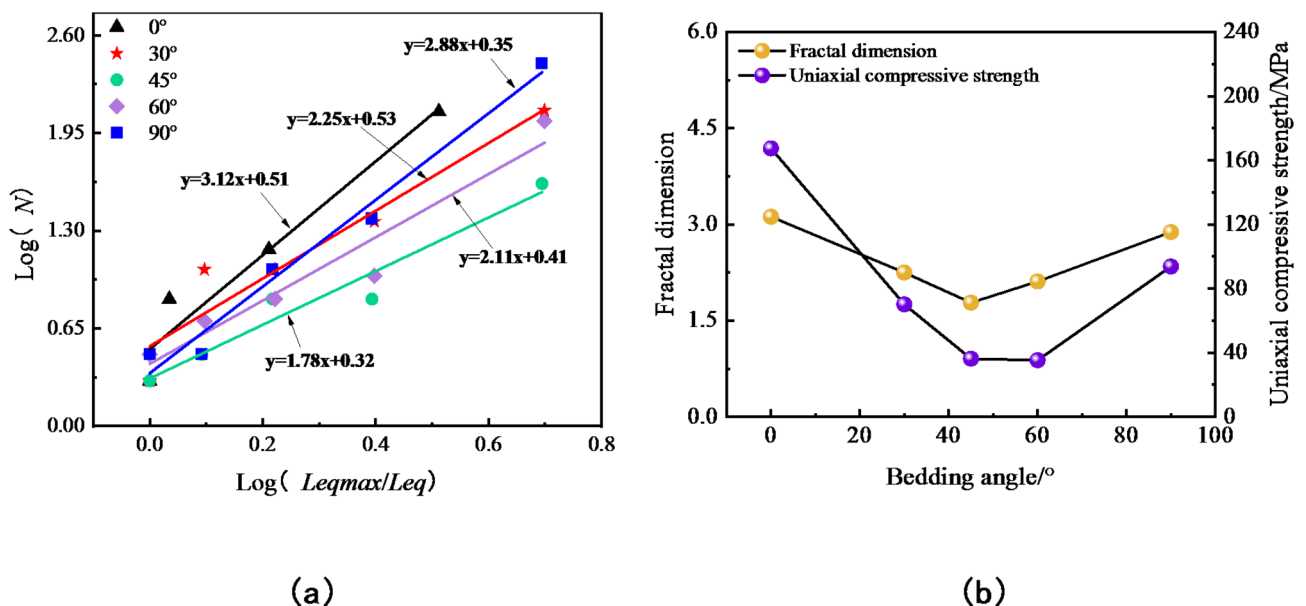
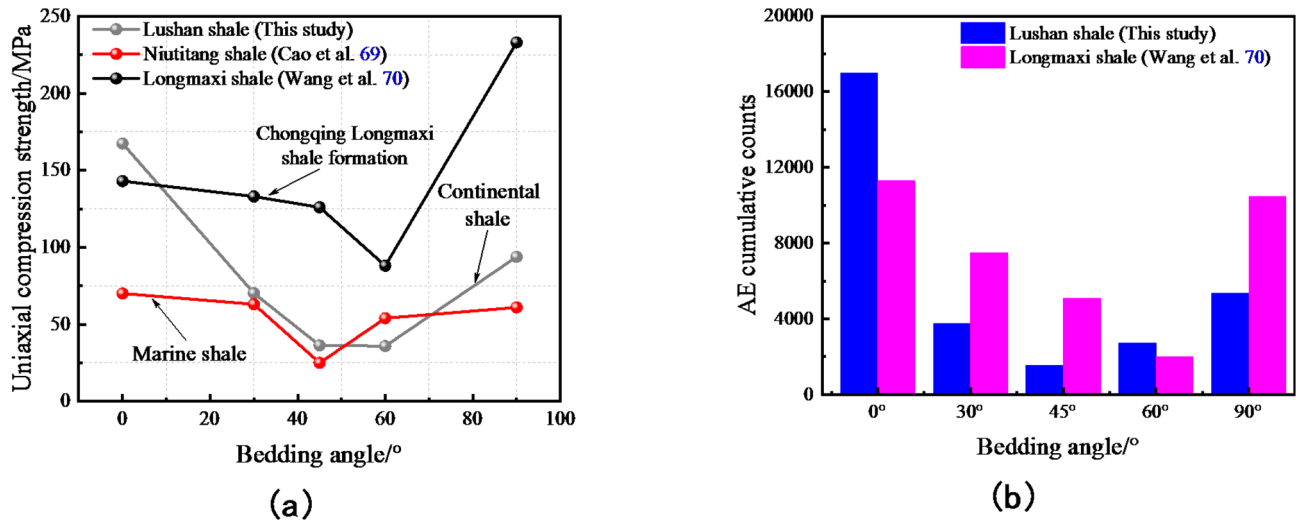


Fig. 15. Fragment fractal parameters: (a)  $\lg(L_{eqmax}/L_{eq})-\lg N$  fitting graph; (b) Fractal dimension, uniaxial compressive strength versus the bedding angles.



**Fig. 16.** Comparison of UCS values (a) and cumulative AE counts (b) between shales sourced from different formations.

shale progressed through a complete linear elastic phase, culminating in a characteristic brittle tensile failure (Type I mode). Conversely, the Lushan shale underwent a compaction stage wherein micro-cracks within the shale underwent either closure or opening (see Fig. 6a). This suggests that the Lushan shale undergoes a distinct failure process from those of Niutitang shale studied by Cao et al.<sup>69</sup>. Furthermore, the UCS of Lushan shale is generally lower than that of Longmaxi shale but higher than Niutitang shale, with the exception of an observed reverse trend at a bedding angle of  $\theta = 60^\circ$  (see Fig. 16a). Shale with reduced porosity and a well-interconnected fracture network typically demonstrates higher UCS values, attributable to the enhanced interlocking between particles and improved load-bearing capacity. Hence, the observed discrepancies in UCS values can be plausibly attributed to variations in porosity and fracture distribution within the shale matrix, which have a substantial impact on the strength properties of the shale. It is important to note that the lowest UCS value was observed within a bedding angle range of  $45^\circ \sim 60^\circ$ . This finding indicates that the effect of bedding angles on UCS can vary depending on the unique characteristics of the shale formations under investigation.

Figure 16b displays the comparison of cumulative AE counts between Lushan shale and Longmaxi shale<sup>70</sup>. Analogous to the variation in UCS values across different bedding angles, the cumulative AE counts also exhibited an initial decline followed by an increase, suggesting a positive correlation between UCS and the cumulative AE counts. However, as illustrated in Fig. 16b, despite the Lushan shale exhibiting the lowest UCS at a bedding angle of  $\theta = 60^\circ$ , this angle does not coincide with the minimum cumulative AE counts. This discrepancy may stem from the existence of natural microcracks and variations in pore distribution within the shale samples, leading to distinct stress concentrations and varied fracture initiation points. As a result, the observed relationship between bedding angle, UCS, and cumulative AE counts may not be entirely uniform, owing to the inherent variations present in the shale specimens.

### Failure mode associated with bedding anisotropy

According to Jaeger's criterion, the failure of rock mass depends on the bedding dip angle and the strength of the material itself. The relationship between the bedding dip angle and the direction of principal stress will directly affect the failure mode. When the bedding angle  $\theta = 60^\circ$ , stress transmission does not concentrate on the bedding plane, and the shear force and normal force on the bedding plane are in a relatively balanced state. This prevents excessive shear slip and significant deformation, and thus the rock mass remains relatively intact (see  $60^\circ$  in Fig. 12).

The RA-AF analysis conducted by Chen et al.<sup>71</sup> disclosed that the failure of shale with bedding angles ranging from  $0^\circ$  to  $30^\circ$  is predominantly governed by the synergistic effect of shear and tensile fractures. In this study, we further established that the proportion of shear cracks augments as the bedding angle is incremented from  $\theta = 45^\circ$  to  $\theta = 90^\circ$  (see Fig. 10). Huang et al.<sup>72</sup> observed that for shale specimens oriented within the range of  $\theta = 30^\circ$  to  $90^\circ$ , a multitude of thin fracture layers emerged in parallel alignment with the lamination, aligning with the layer-slip failure mode observed specifically at  $\theta = 30^\circ$  to  $60^\circ$ . Table 3 comprehensively summarizes the prevalent failure modes of shale identified in this study, as well as those reported in the existing literature. The failure modes of shale observed across various bedding angles were overall consistent with those reported by Cao et al.<sup>69</sup> and Wang et al.<sup>70</sup>. However, at  $\theta = 45^\circ$ , both this study and Cao et al.<sup>69</sup> demonstrated a layer-slip failure mode, whereas Wang et al.<sup>70</sup> observed a distinctive combination of tensile and shear failure modes. This may arise from different shale structures and properties influenced by various sedimentary environments and sampling locations<sup>73,74</sup>.

The failure mode of rock is not only affected by loading conditions, but also closely related to microstructure, mineral composition and porosity. Although in the process of sampling and processing, the difference of the sample and the error caused by processing cannot be avoided, so we combined the measured wave velocity

Bedding angle ( $\theta$ )	Failure mode	References
0°	Through-layer failure with horizontal bedding cracks	This study
	Tension splitting along the bedding plane	Wang et al. <sup>70</sup>
	Through-layer failure	Cao et al. <sup>69</sup>
30°	Layer-slip failure with transverse secondary cracks	This study
	Shear sliding failure	Wang et al. <sup>70</sup>
	Through-layer shear-slip failure	Cao et al. <sup>69</sup>
45°	Layer-slip failure with vertical splitting cracks	This study
	Shear failure of crossing and along bedding	Wang et al. <sup>70</sup>
	Layer-slip failure	Cao et al. <sup>69</sup>
60°	Layer-slip failure with parallel secondary cracks	This study
	Shear failure of crossing and along bedding	Wang et al. <sup>70</sup>
	Through-layer shear-slip failure	Cao et al. <sup>69</sup>
90°	Tensile splitting failure with local shear cracks	This study
	Tension failure crosses the matrix and shear sliding along the bedding plane	Wang et al. <sup>70</sup>
	Through-layer shear-slip failure	Cao et al. <sup>69</sup>

**Table 3.** Comparison table of different bedding angles failure modes.

data to carry out a simple classification of the sample. Through the measurement of wave velocity, samples with similar wave velocity can be selected to reduce the data discreteness caused by the difference of rock samples and improve the comparability of test results.

In some samples, failure may occur along the bedding direction, while in others, it may manifest as a complex pattern of crack propagation, even though entire sections of the rock (see Fig. 12). This difference indicates that the failure modes of anisotropic rocks have different complexity and diversity. Failure modes in experiments are often limited by test conditions, and some failure modes may only appear under specific loading modes and stress fields. Stress distribution and loading modes in real engineering environments tend to have more uncertainty and may lead to different failure behaviors<sup>75–79</sup>. Compared with the findings of previous research, the failure patterns of anisotropic shale observed in this study is generally consistent with previous findings (see Table 3). In order to accurately simulate in-situ rock deformation and failure characteristics, it is necessary to integrate more factors such as temperature, pore pressure, confining pressure, fault or natural fracture distribution, and the process will be more complicated. However, the real inversion of this process is not the focus of this paper, and can be further studied by using experimental and numerical simulation methods in the future.

#### *Fractal comparison of between AE counts and fracture fragments*

A robust correlation exists between the microscopic fracture response, as interpreted through AE counts, and the macroscopic failure mode, as derived from fragment statistical analysis. As shown in Fig. 17, the fractal dimension of fracture fragments is compared with the cumulative AE counts, including cumulative AE counts, the maximum AE count and the peak  $b$ -value, respectively. When the bedding plane aligns either perpendicularly ( $\theta=0^\circ$ ) or parallel ( $\theta=90^\circ$ ) to the loading direction, the fractal dimension of the fragments, along with the maximum AE counts and cumulative AE counts, generally exceed those observed in shale with inclined bedding planes. Furthermore, the maximum AE count and cumulative AE counts typically exhibit an upward trend with the increase in fractal dimension, suggestive of a positive relationship between the complexity of fractal fragments and the occurrence of AE events. However, a fluctuating trend in peak  $b$ -value is observed across different bedding angles in shales with inclined bedding planes. At  $\theta=60^\circ$ , a higher peak  $b$ -value is associated with a relatively lower fractal dimension, whereas at  $\theta=30^\circ$ , a lower peak  $b$ -value is observed alongside a larger fractal dimension. This observation suggests that there is no direct, straightforward correlation between the peak  $b$ -value and the fractal dimension of the fracture fragments. The fractal dimension of the fragment provides a holistic view of the entire loading process, whereas the peak  $b$ -value captures a snapshot of the time when the proportion of small damage cracks reaches its maximum. Subsequent to attaining the peak  $b$ -value, the specimen remains under loading, leading to continuous crack evolution that may subsequently alter the fractal characteristics of the fracture fragments.

Given that macroscopic cracks emerged in stage IV, significantly influencing the transmission of AE signals, stage III in Fig. 10 was specifically chosen for the analysis of the fractal dimension of AE counts. As shown in Fig. 18, when the bedding angle varies from  $\theta=0^\circ$  to  $\theta=60^\circ$ , a positive correlation is observed between the  $D_{AE}$  and that of the fragments. In contrast, at  $\theta=90^\circ$ , the fragments exhibit the highest fractal dimension, whereas the AE displays the lowest fractal dimension. As the loading direction is perpendicular to the bedding planes, the bedding surface is able to withstand higher stress levels during the loading process compared to other orientations. As a result, there are fewer small damage cracks generated, leading to a smaller fractal dimension of acoustic emission. Among the various bedding angles, the highest cumulative AE counts, maximum AE counts and  $D_{AE}$  are all observed at a bedding inclination angle of  $\theta=0^\circ$ . This observation indicates that as the specimen undergoes damage, there is a greater release of energy, which triggers the activation of the bedding plane. This, in turn, leads to the production of more fractured fragments and contributes to a larger fractal dimension. Drawing from these observations, it can be definitively concluded that there exists a robust correlation between the failure

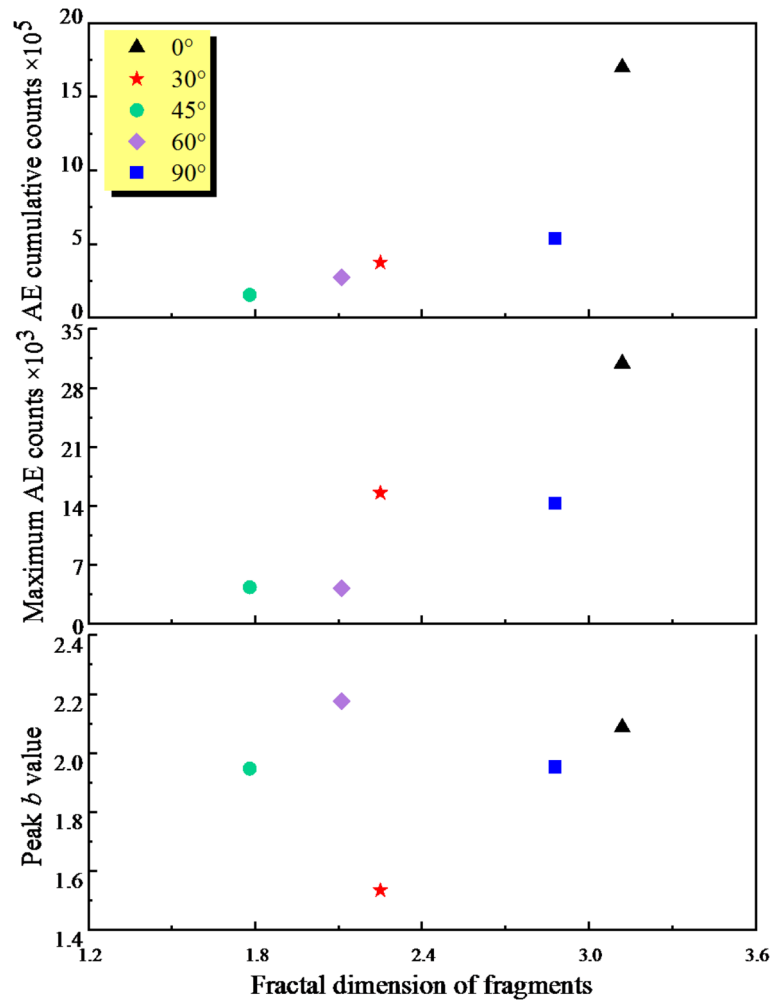


**Fig. 17.** The relationship between the fractal dimension of the fragment and the characteristic parameters of acoustic emission.

mode and the fractal AE events within the bedding angle range of  $\theta=0^\circ$  to  $\theta=60^\circ$ . The elevated AE counts and enlarged fractal dimension serve as indicators of a more extensive fracturing process and a heightened level of energy release during the failure event. Furthermore, the existence and orientation of bedding planes play a pivotal role in shaping the failure behavior of the shale specimen. At higher bedding inclination angles, such as  $\theta=90^\circ$ , the activation of the bedding plane and the resultant fracturing yield a less discernible and correlated AE response.

### Practical significance and limitations

This study provides practical insights into the mechanical behavior and failure characteristics of Lushan shale, which is crucial for optimizing hydraulic fracturing, improving rock stability assessments, and enhancing resource extraction efficiency. The “V”-shaped trend of UCS and AE counts with bedding angles highlights the weakest structural orientation ( $\theta=60^\circ$ ), offering a reference for selecting fracture initiation angles in hydraulic fracturing operations. The identification of a sharp drop in the AE b-value at 70–80% UCS as a precursor to rock instability provides a potential early warning indicator for monitoring shale failure. Furthermore, the dominant role of tensile cracks (over 70%) in compressive failure suggests that hydraulic fracturing strategies should focus on promoting tensile crack propagation for effective reservoir stimulation. Based on the fractal statistical analysis, for bedding angle lower than  $60^\circ$ , there is a positive correlation between the fractal dimensions of AE signals and shale fragment distribution. The correlation further links micro-fracture processes to macroscopic failure patterns, aiding in the design of more efficient and controlled fracturing techniques. These findings are helpful to deepen the understanding of rock mechanical behavior, promote the development of related disciplines, and provide practical cases for the development of shale gas in Lushan area.

However, the lab testing of anisotropic rocks is controversial and uncertain, largely due to variations in rock properties, testing methodology, ambient stress conditions, temperature and water saturation<sup>14–16,75–79</sup>. This study focuses on the compression behavior of anisotropic shale, combined with acoustic emission techniques, to investigate its fracture mechanisms. To mitigate the uncertainties caused by bedding anisotropy in future research, it is essential to adopt a multi-scale and multi-field approach by including advanced imaging techniques, such

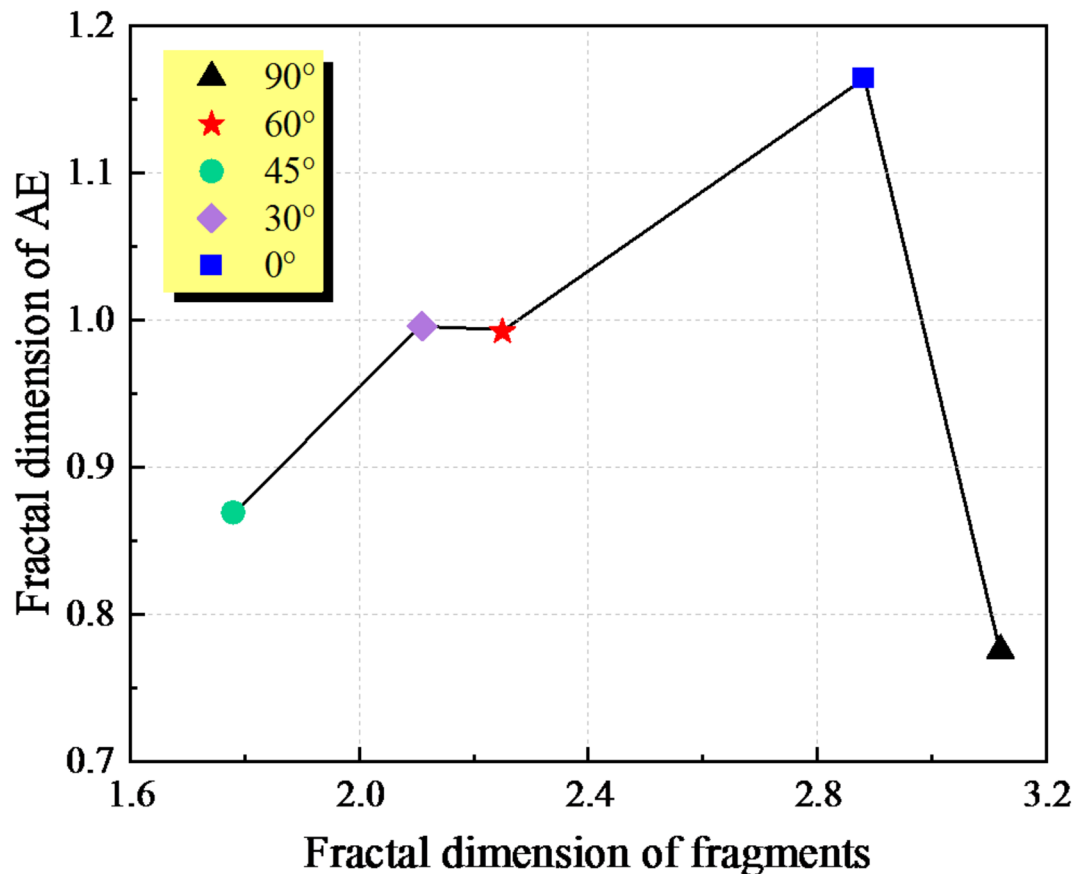


**Fig. 18.** Relationship between the fractal dimension of fragments and the fractal dimension of acoustic emission.

as micro-CT or SEM, to capture microscale structural heterogeneities, and performing systematic tests under controlled conditions that simulate in-situ stress, temperature, and fluid saturation. Additionally, developing numerical models calibrated with experimental data can help quantify the influence of bedding anisotropy and predict crack evolution under different scenarios. Furthermore, the influence of micro-pores under compression was not taken into account when combining acoustic emission with uniaxial tests. During the initial first stage of acoustic emission (compaction stage), if pores account for a large proportion, they will affect the number of AE events. The initial stage of acoustic emission is the combined effect of pore compaction, weak structural planes, and microcrack initiation. This study did not consider the influence of micro aspects, which is a direction we need to explore in the future.

### Conclusions

In this study, a series of compression tests in conjunction with acoustic emission monitoring were conducted on Lushan shale with varying bedding angles to explore the fracture evolution and fractal failure process of anisotropic rock. Based on a comprehensive evaluation of failure mode in relation to shale anisotropy, the following conclusions were reached:

- (1) The uniaxial compressive strength and cumulative acoustic emission counts exhibit a “V” shaped trend with increasing bedding dip angle. At bedding angle ( $\theta$ ) = 60°, the average uniaxial compressive strength (UCS) reaches its minimum of 35.867 MPa among the five angles.
- (2) Through acoustic emission analysis, a sharp drop greater than 0.5 in  $b$ -value occurs at 70–80% UCS, indicating rock instability. The tensile cracks playing a crucial role (accounting for greater than 70%) in Lushan shale’s compressive failure.
- (3) The failure modes of shale mainly include through-layer failure, layer-slip failure, and tensile splitting failure. The macroscopic failure patterns of shale samples with different bedding angles are consistent with the distribution characteristics of RA-AF values.
- (4) The number of AE events increases with the increase of the fractal dimension of shale fragments, but it is opposite at  $\theta$  = 90°, indicating that the macro failure mode of shale is related to the micro-fracture process. The study of anisotropic crack evolution and fractal failure mechanisms provides insights into the design of hydraulic fracturing operations related to Lushan shale.

## Data availability

The data that support the findings of this study will be made available from the corresponding author upon reasonable request.

Received: 31 October 2024; Accepted: 14 April 2025

Published online: 24 April 2025

## References

- Wu W, Wang T, Bai J, Liu J, Wang X, Xu H, Feng G. Failure Characteristics and Cooperative Control Strategies for Gob-Side Entry Driving near an Advancing Working Face: A Case Study. *Processes*, **12**, 1398. <https://doi.org/10.3390/pr12071398> (2024).
- Kolawole, O. & Opong, F. Assessment of inherent heterogeneity effect on continuous mechanical properties of shale via uniaxial compression and scratch test methods[J]. *Rock Mech. Bull.* **2** (4), 100065. <https://doi.org/10.1016/j.rockmb> (2023). 2023.100065.
- Cook N G W. The failure of rock[C]//International journal of rock mechanics and mining sciences & geomechanics abstracts. *Pergamon* **2** (4), 389–403. [https://doi.org/10.1016/0148-9062\(65\)90004-5](https://doi.org/10.1016/0148-9062(65)90004-5) (1965).
- Zhao, Y., Bi, J., Wang, C. et al. Effect of Unloading Rate on the Mechanical Behavior and Fracture Characteristics of Sandstones Under Complex Triaxial Stress Conditions. *Rock Mech Rock Eng* **54**, 4851–4866. <https://doi.org/10.1007/s00603-021-02515-x> (2021).
- Kaiser, P. K., Amann, F. & Steiner, W. How highly stressed brittle rock failure impacts tunnel design[C]//ISRM EUROCK. ISRM, : ISRM-EUROCK-2010-003. (2010). <https://doi.org/10.1201/b10550-5>
- Amann, F. et al. Experimental study of the brittle behavior of clay shale in rapid unconfined compression[J]. *Rock Mech. Rock Eng.* **44**, 415–430. <https://doi.org/10.1007/s00603-011-0156-3> (2011).
- Zhao Y, Wang CL, Ning L, Zhao HF, Bi J. Pore and fracture development in coal under stress conditions based on nuclear magnetic resonance and fractal theory. *Fuel*. **309**, 122112. <https://doi.org/10.1016/j.fuel.2021.122112> (2022).
- Li, G. et al. Shear creep mechanical properties and damage model of mudstone in open-pit coal mine[J]. *Sci. Rep.* **12** (1), 5148. <https://doi.org/10.1038/s41598-022-08488-3> (2022).
- Gong, J. et al. An integrated assessment system for shale gas resources associated with graptolites and its application[J]. *Appl. Energy*. **262**, 114524. <https://doi.org/10.1016/j.apenergy.2020.114524> (2020).
- Zhao, C. et al. *Investigation on Mechanical Properties, AE Characteristics, and Failure Modes of Longmaxi Formation Shale in Changning, Sichuan Basin, China*[J]561239–1272 (*Rock Mechanics and Rock Engineering*, 2023a). <https://doi.org/10.1007/s00603-022-03130-0>
- Zhao, C. et al. Mechanical responses and failure characteristics of longmaxi formation shale under real-time high temperature and high-stress coupling[J]. *Eng. Fail. Anal.* **152**, 107490. <https://doi.org/10.1016/j.engfailanal.2023.107490> (2023b).
- Zhao, G. et al. Anisotropic mechanical behavior of ultra-deep shale under high in-situ stress, a case study in the Luzhou block of the Southern Sichuan basin, China[J]. *Int. J. Rock Mech. Min. Sci.* **170**, 105536. <https://doi.org/10.1016/j.ijrmm.2023.105536> (2023c).
- Zhao, Y., Wang, C.L. & Bi, J. Analysis of Fractured Rock Permeability Evolution Under Unloading Conditions by the Model of Elastoplastic Contact Between Rough Surfaces. *Rock Mech Rock Eng* **53**, 5795–5808. <https://doi.org/10.1007/s00603-020-02224-x> (2020).
- Cai, M. Rock mass characterization and rock property variability considerations for tunnel and cavern design[J]. *Rock Mech. Rock Eng.* **44**, 379–399. <https://doi.org/10.1007/s00603-011-0138-5> (2011).
- Pandit, B. et al. Probabilistic characterization of rock mass from limited laboratory tests and field data: associated reliability analysis and its interpretation[J]. *Rock Mech. Rock Eng.*, **52**: 2985–3001. <https://doi.org/10.1007/s00603-019-01780-1> (2019).
- Mazraehli, M. & Zare, S. Application of different stochastic numerical procedures in rock tunnel lining design[J]. *Arab. J. Geosci.* **15** (18), 1490. <https://doi.org/10.1007/s12517-022-10710-5> (2022).
- Huang, Y. et al. Review of the productivity evaluation methods for shale gas wells[J]. *J. Petroleum Explor. Prod. Technol.* **14** (1), 25–39. <https://doi.org/10.1007/s13202-023-01698-z> (2024).
- Ardebili, P. N., Jozanikohan, G. & Moradzadeh, A. Estimation of porosity and volume of shale using artificial intelligence, case study of Kashafud gas reservoir, NE Iran[J]. *J. Petroleum Explor. Prod. Technol.* **14** (2), 477–494. <https://doi.org/10.1007/s13202-023-01729-9> (2024).
- Yang, X. et al. Numerical experimental study on the fracture process of shale containing internal prefabricated cracks based on CT scanning with different quartz contents[J]. *J. Petroleum Explor. Prod. Technol.* **1**–18. <https://doi.org/10.1007/s13202-024-01867-8> (2024).
- Esatyana, E., Alipour, M. & Sakhaee-Pour, A. Characterizing anisotropic fracture toughness of shale using nanoindentation[J]. *SPE Reservoir Eval. Eng.* **24** (03), 590–602. <https://doi.org/10.2118/205488-PA> (2021).
- Deng Q, Schmittbuhl J, Cacace M, Blöcher G, Mechanical stiffness and permeability of a reservoir-scale rough fracture during closure. *J Geophys Res-Solid Earth* 129:e2024JB029001 (2024).
- Suo Y, Zhao Y J, Fu X F, et al. Study on fracture propagation behavior of deep high-temperature shale gas based on the modified MERR criterion[J]. *Theoretical and Applied Fracture Mechanics*, **131**, 104352 (2024).
- Jiang, T. et al. Volume fracturing of deep shale gas horizontal wells[J]. *Natural Gas Industry B*, **4**(2): 127–133. (2017). <https://doi.org/10.1016/j.ngib.2017.07.018>.
- Zhang, Y. et al. Acoustic emission evolution and hydraulic fracture morphology of Changning shale stressed to failure at different injection rates in the laboratory[J]. *Rock Mech. Rock Eng.* **57** (2), 1287–1308. <https://doi.org/10.1007/s00603-023-03586-8> (2023a).
- Zhang, Y. et al. Mutual impact of true triaxial stress, borehole orientation and bedding inclination on laboratory hydraulic fracturing of Lushan shale[J]. *J. Rock Mech. Geotech. Eng.* **15** (12), 3131–3147. <https://doi.org/10.1016/j.jrmge.2023.02.015> (2023b).
- Zhang, Y. et al. Combined effects of bedding anisotropy and matrix heterogeneity on hydraulic fracturing of shales from Changning and Lushan, South China: an experimental investigation[J]. *J. Asian Earth Sci.* **259**, 105908. <https://doi.org/10.1016/j.jseaes.2023.105908> (2023c).
- Zhao, Y. et al. Investigation on model-I fracture toughness of sandstone with the structure of typical bedding inclination angles subjected to three-point bending[J]. *Theoret. Appl. Fract. Mech.* **119**, 103327. <https://doi.org/10.1016/j.tafmec.2022.103327> (2022a).
- Zhang, Y. et al. Impacts of wellbore orientation with respect to bedding inclination and injection rate on laboratory hydraulic fracturing characteristics of Lushan shale[J]. *Fuel*, **353**: 129220. (2023). <https://doi.org/10.1016/j.fuel.2023.129220>.
- Wu, S. V., Gan, Y. X., Ren, Y. & Zheng, L. F. Feasibility of acoustic emission indexes based on RA and AF values in tunnel monitoring. *Chin. J. Eng.* **42**, 723–730. <https://doi.org/10.13374/j.issn2095-9389.2019.06.28.001+> (2020).
- Horsrud, P. Estimating mechanical properties of shale from empirical correlations[J]. *SPE Drill. Completion.* **16** (02), 68–73. <https://doi.org/10.2118/56017-PA> (2001).
- Suo Y, Dong M, Fu X, et al. Experimental and numerical simulation research on hot dry rock wellbore stability under different cooling methods[J]. *Geothermics*, **119**: 102977 (2024).

32. Koncagül, E. C. & Santi, P. M. Predicting the unconfined compressive strength of the breathitt shale using slake durability, shore hardness and rock structural properties[J]. *Int. J. Rock Mech. Min. Sci.* **36** (2), 139–153. [https://doi.org/10.1016/S0148-9062\(98\)00174-0](https://doi.org/10.1016/S0148-9062(98)00174-0) (1999).
33. Niu, Y., Zhou, X. P. & Berto, F. Evaluation of fracture mode classification in flawed red sandstone under uniaxial compression[J]. *Theoret. Appl. Fract. Mech.* **107**, 102528. <https://doi.org/10.1016/j.tafmec.2020.102528> (2020).
34. Zhao, C. et al. Investigation on the mechanical behavior, permeability and failure modes of limestone rock under stress-seepage coupling[J]. *Eng. Fail. Anal.* **140**, 106544. <https://doi.org/10.1016/j.engfailanal.2022.106544>.
35. Ohtsu, M. (ed) Acoustic emission and related non-destructive evaluation techniques in the fracture mechanics of concrete: fundamentals and applications. Woodhead Publishing, (2020). <https://doi.org/10.1016/B978-1-78242-327-0.180> 01–8.
36. Sagasta, F. et al. Acoustic emission energy b-value for local damage evaluation in reinforced concrete structures subjected to seismic loadings[J]. *Mech. Syst. Signal Process.* **102**, 262–277. <https://doi.org/10.1016/j.ymsp.2017.09.022> (2018).
37. Guo, P. et al. Effects of thermally-induced cracks on acoustic emission characteristics of granite under tensile conditions[J]. *Int. J. Rock Mech. Min. Sci.* **144**, 104820. <https://doi.org/10.1016/j.ijrmms.2021.104820> (2021).
38. Gan, Y. X. Research on characterization of acoustic emission parameters of underground engineering rock mass rupture and optimization of positioning method. (2007). <https://doi.org/10.26945/d.cnki.gbjku.2020.000139>
39. Zhang, S. W. et al. Fractal characteristics and acoustic emission of anisotropic shale in Brazilian tests[J]. *Tunn. Undergr. Space Technol.* **71**, 298–308. <https://doi.org/10.1016/j.tust.2017.08.031> (2018).
40. Grassberger, P. Generalized dimensions of strange attractors[J]. *Phys. Lett. A.* **97** (6), 227–230. [https://doi.org/10.1016/0375-9601\(83\)90753-3](https://doi.org/10.1016/0375-9601(83)90753-3) (1983a).
41. Grassberger, P. & Procaccia, I. Characterization of strange attractors[J]. *Phys. Rev. Lett.* **50** (5), 346. <https://doi.org/10.1103/PhysRevLett.50.346> (1983b).
42. Grassberger, P. & Procaccia, I. Measuring the strangeness of strange attractors[J]. *Phys. D: Nonlinear Phenom.* **9** (1–2), 189–208. [https://doi.org/10.1016/0167-2789\(83\)90298-1](https://doi.org/10.1016/0167-2789(83)90298-1) (1983c).
43. Zhu, H. & Ji, C. C. *Fractal Theory and its Applications*pp. 22–53 (Science, 2010).
44. Wang, G. F. *Study on Characteristics of Kaiser Signal of Acoustic Emission in Rock*67–68 (Jiangxi university of science and technology, 2007).
45. Wang CL, Zhao Y, Ning L, Bi J. Permeability evolution of coal subjected to triaxial compression based on in-situ nuclear magnetic resonance. *Int J Rock Mech Min Sci.* **159**, 105213 (2022)
46. He, M. C., Yang, G. X., Miao, J. L., Jia, X. N. & Jiang, T. T. Classification and research methods of rockburst experimental fragments. *Chinese Journal of Rock Mechanics and Engineering*, 28: 1521–1529 (2009). <https://doi.org/10.3321/j.issn:1000-6915.2009.08.002>.
47. Huang, D., Tan, Q. & Huang, R. Q. Fractal characteristics of fragmentation and correlation with energy of marble under unloading with high confining pressure. *Chin. J. Rock Mech. Eng.* **31**, 1379–1389. <https://doi.org/10.3969/j.issn.1000-6915.2012.07.010> (2012).
48. Zhao, Y., Liu, HH. An Elastic Stress–Strain Relationship for Porous Rock Under Anisotropic Stress Conditions. *Rock Mech Rock Eng* **45**, 389–399. <https://doi.org/10.1007/s00603-011-0193-y> (2012)
49. Deng, Y. et al. Theoretical analysis and experimental research on the energy dissipation of rock crushing based on fractal theory[J]. *J. Nat. Gas Sci. Eng.* **33**, 231–239. <https://doi.org/10.1016/j.jngse.2016.05.020> (2016).
50. Okubo, S., Nishimatsu, Y. & Sciences Uniaxial compression testing using a linear combination of stress and strain as the control variable[C]//International Journal of Rock Mechanics and Mining *Geomech. Abstracts Pergamon*, 22(5): 323–330. [https://doi.org/10.1016/0148-9062\(85\)92064-9](https://doi.org/10.1016/0148-9062(85)92064-9) (1985).
51. Darvell, B. W. Uniaxial compression tests and the validity of indirect tensile strength [J]. *J. Mater. Sci.* **25** (2), 757–780. <https://doi.org/10.1007/BF03372161> (1990).
52. Cai, M. Practical estimates of tensile strength and Hoek–Brown strength parameter  $M_i$  of brittle rocks[J]. *Rock Mech. Rock Eng.* **43** (2), 167–184. <https://doi.org/10.007/s00603-009-0053-1> (2010).
53. Zhong, J. et al. Macro-fracture mode and micro-fracture mechanism of shale[J]. *Pet. Explor. Dev.* **42** (2), 269–276 (2015).
54. Liu, S., Wang, Z. & Zhang, L. Experimental study on the cracking process of layered shale using X-ray microCT[J]. *Energy Explor. Exploit.* **36** (2), 297–313. <https://doi.org/10.1177/0144598717736855> (2018).
55. Li, G. et al. An unsteady creep model for a rock under different moisture contents[J]. *Mech. Time-Dependent Mater.* **27** (2), 291–305. <https://doi.org/10.1007/s11043-022-09561-0> (2023).
56. Fakhimi, A. & Hemami, B. Axial splitting of rocks under uniaxial compression[J]. *Int. J. Rock Mech. Min. Sci.* **79**, 124–134. <https://doi.org/10.1016/j.ijrmms.2015.08.013> (2015).
57. Cavalieri, K. M. V. et al. Determination of precompression stress from uniaxial compression tests[J]. *Soil Tillage. Res.* **98** (1), 17–26. <https://doi.org/10.1016/j.still.2007.09.020> (2008).
58. Edris, W. F., Al-Fhaid, H. & Al-Tamimi, M. Evolution of durability and mechanical behaviour of mud mortar stabilized with oil shale Ash, lime, and cement[J]. *Civ. Eng. J.* **9**, 2175–2192. <https://doi.org/10.28991/cej-2023-09-09-06> (2023).
59. Eberhardt, E., Stead, D. & Stimpson, B. Quantifying progressive pre-peak brittle fracture damage in rock during uniaxial compression[J]. *Int. J. Rock Mech. Min. Sci.* **36** (3), 361–380. [https://doi.org/10.1016/S0148-9062\(99\)00019-4](https://doi.org/10.1016/S0148-9062(99)00019-4) (1999).
60. Fjær, E. & Nes, O. M. The impact of heterogeneity on the anisotropic strength of an outcrop shale[J]. *Rock Mech. Rock Eng.* **47**, 1603–1611. <https://doi.org/10.1007/s00603-014-0598-5> (2014).
61. Bu, J. et al. Experimental study on crack propagation of concrete under various loading rates with digital image correlation method[J]. *Int. J. Concrete Struct. Mater.* **14**, 1–25. <https://doi.org/10.1186/s40069-020-00400-5> (2020).
62. Sun, X. et al. The Mechanical Properties and Fracture Characteristics of Shale Layered Samples from the Lucaogou Formation Considering Natural Crack and Mineral Distribution[J]. *Materials*, **16**(17): 5881. <https://doi.org/10.3390/ma16175881> (2023).
63. Cui, J. et al. New Advances in Shale Porosity Research [J]. *Advances in Earth Science*, 27(12): 1319. (2012). <https://doi.org/10.1186/7/j.issn.1001-8166>. 2012.12.1319.
64. Bieniawski, Z. T. & Sciences Mechanism of brittle fracture of rock: part I—theory of the fracture process[C]//International Journal of Rock Mechanics and Mining *Geomech. Abstracts Pergamon*, 4(4): 395–406. [https://doi.org/10.1016/0148-9062\(67\)90030-7](https://doi.org/10.1016/0148-9062(67)90030-7) (1967).
65. Lajtai, E. Z. & Lajtai, V. N. The evolution of brittle fracture in rocks[J]. *J. Geol. Soc.* **130** (1), 1–16. <https://doi.org/10.1144/gsjgs.130.1.0001> (1974).
66. Diederichs, M. S. Manuel Rocha medal recipient rock fracture and collapse under low confinement conditions[J]. *Rock Mech. Rock Eng.* **36**, 339–381. <https://doi.org/10.1007/s00603-003-0015-y> (2003).
67. Gao, M. et al. Mechanical characterization of uniaxial compression associated with lamination angles in shale[J]. *Adv. Geo-Energy Res.*, **13**(1). (2024).
68. Aggelis, D. G. Classification of cracking mode in concrete by acoustic emission parameters[J]. *Mech. Res. Commun.* **38** (3), 153–157. <https://doi.org/10.1016/j.mechrescom.2011.03.007> (2011).
69. Cao, H. et al. Experimental investigation on anisotropic characteristics of marine shale in Northwestern Hunan, China[J]. *J. Nat. Gas Sci. Eng.* **81**, 103421. <https://doi.org/10.1016/j.jngse.2020.103421> (2020).
70. Wang, Y., Li, C. H. & Hu, Y. Z. Experimental investigation on the fracture behaviour of black shale by acoustic emission monitoring and CT image analysis during uniaxial compression[J]. *Geophys. J. Int.* **213** (1), 660–675. <https://doi.org/10.1093/gji/ggy011> (2018).

71. Chen, B. et al. Experiment study on damage properties and acoustic emission characteristics of layered shale under uniaxial compression[J]. *Materials* **16** (12), 4317. <https://doi.org/10.3390/ma16124317> (2023).
72. Huang, B. et al. Investigating the meso-mechanical anisotropy and fracture surface roughness of continental shale[J]. *J. Geophys. Research: Solid Earth*. **125** (8). <https://doi.org/10.1029/2019JB017828> (2020). e2019JB017828.
73. Yan, J. F. et al. Geochemical and geological characteristics of the lower cambrian shales in the middle–upper Yangtze area of South China and their implication for the shale gas exploration[J]. *Mar. Pet. Geol.* **70**, 1–13. <https://doi.org/10.1016/j.marpetgeo.2015.11.010> (2016).
74. Li, G. et al. Main controlling factor and mechanism of gas-in-place content of the lower cambrian shale from different sedimentary facies in the Western Hubei area, South China[J]. *Pet. Sci.* **21** (3), 1488–1507 (2024).
75. Li, Zongze, Kang Yanfei, Fan Jinyang, Fourmeau Marion, Chen Jie, Jiang Deyi, Nelias Daniel. Macroscopic experimental study and microscopic phenomenon analysis of damage self-healing in salt rock. *Engineering Geology*, 107634 (2024).
76. Deng Q, Shangguan J, Ji Y et al. Relating normal stiffness to permeability of a deformed self-affine rough fracture using its geometric properties. *J Rock Mech Geotech Eng* <https://doi.org/10.1016/j.jrmge.2024.05.008> (2024).
77. Li, W., Wang, X. & Cheng, J. Measurement of the anisotropic elastic properties of shale: uncertainty analysis and water effect[J]. *Bull. Eng. Geol. Environ.* **78**, 6075–6087. <https://doi.org/10.1007/s10064-019-01517-y> (2019).
78. Li, Zongze, Fan Jinyang, Fourmeau Marion, Chen Jie, Jiang Deyi, Nelias Daniel. Long-term deformation of rock salt under creep–fatigue stress loading paths: Modeling and prediction. *International Journal of Rock Mechanics and Mining Sciences*, **181**, 105861(2024).
79. Mazraehli, M. & Zare, S. Probabilistic Estimation of rock load acting on tunnels considering uncertainty in peak and post-peak strength parameters[J]. *Geotech. Geol. Eng.* **40** (5), 2719–2736. <https://doi.org/10.1007/s10706-022-02057-1> (2022).

## Acknowledgements

This research was supported by National Natural Science Foundation of China (No. 52464005), the Youth Talent Growth Project of Guizhou Provincial Department of Education (No. QianJiaoJi[2024]18), Basic Research Project of Guizhou University (No. [2023]40), Guizhou Provincial Basic Research Program (Natural Science) (No. QianKeHeJiChu-ZK [2024]YiBan011), and Research Fund for Talents of Guizhou University (No. GuiDaRenJiHeZi(2023)24).

## Author contributions

Huasen Huang: Investigation, Methodology, Performing experiment, Writing-Original Draft. Yu Zhou: Project administration, Funding acquisition. Yongfa Zhang: Methodology, Resources, New diagrams and interpretation of results, Writing-Review & Editing. Chunlin Wang: Investigation, Performing experiment. Jin Bi: Investigation, Performing experiment.

## Declarations

### Competing interests

The authors declare no competing interests.

## Additional information

**Supplementary Information** The online version contains supplementary material available at <https://doi.org/10.1038/s41598-025-98695-5>.

**Correspondence** and requests for materials should be addressed to Y.Z.

**Reprints and permissions information** is available at [www.nature.com/reprints](http://www.nature.com/reprints).

**Publisher's note** Springer Nature remains neutral with regard to jurisdictional claims in published maps and institutional affiliations.

**Open Access** This article is licensed under a Creative Commons Attribution-NonCommercial-NoDerivatives 4.0 International License, which permits any non-commercial use, sharing, distribution and reproduction in any medium or format, as long as you give appropriate credit to the original author(s) and the source, provide a link to the Creative Commons licence, and indicate if you modified the licensed material. You do not have permission under this licence to share adapted material derived from this article or parts of it. The images or other third party material in this article are included in the article's Creative Commons licence, unless indicated otherwise in a credit line to the material. If material is not included in the article's Creative Commons licence and your intended use is not permitted by statutory regulation or exceeds the permitted use, you will need to obtain permission directly from the copyright holder. To view a copy of this licence, visit <http://creativecommons.org/licenses/by-nc-nd/4.0/>.

© The Author(s) 2025